https://doi.org/10.5194/egusphere-2026-2992
Preprint. Discussion started: 24 June 2026

Flood dynamics driven by multiple levee breaches: two-dimensional hydrodynamic–morphodynamic modelling of the 16–19 May 2023 Senio River event (Italy)

Francesca Aureli[1], Sara Carta[1], Susanna Dazzi[1], Paolo Mignosa[1]

[1]Department of Engineering and Architecture, University of Parma, Parma, 43124, Italy

Correspondence to: Francesca Aureli (francesca.aureli@unipr.it)

Abstract. The extreme rainfall event that affected the Emilia-Romagna region (Italy) between 16 and 17 May 2023 triggered widespread flooding and multiple levee breaches along the Senio River, leading to extensive inundation of agricultural and peri-urban areas. This study presents a high-resolution two-dimensional (2D) hydrodynamic model based on the parallel GPU-accelerated solver PARFLOOD, coupled with a morphodynamic model to explicitly simulate multiple levee breach formation and evolution during the May 2023 event. The model reconstructs the flood wave using observed hydrometric data and consistent hydraulic boundary conditions. A grid resolution of 1 m enables detailed representation of breach widening, crest lowering, erosion dynamics, and inundation processes. The modelling framework allows quantitative assessment of overflow volumes, flood extent, water depth distribution, and flood arrival times, and is supported by a comprehensive dataset including hydrometric records, high-resolution pre- and post-event topography, flood extent mapping, and eyewitness observations. Results show that morphodynamic feedback strongly controls flood volume partitioning and inundation timing. A substantial portion of the total flood volume is released through breaches; however, return-flow breaches are also observed, whereby part of the water previously spilled into the inundated areas re-enters the river channel. This behaviour leads to complex hydraulic interactions between the river and the surrounding areas, including non-monotonic discharge evolution along the river reach. The analysis highlights the importance of multiple simultaneous levee breaches, a condition that is rarely documented in the literature and challenges traditional flood hazard assessment approaches based on independent breach scenarios. The study shows that a physically based breach approach, coupled with a 2D shallow water model, provides a robust framework for flood reconstruction and offers new insights for residual flood risk assessment in embanked low-gradient river systems.

1 Introduction

Levees are among the most widely implemented structural flood mitigation measures in lowland river systems worldwide. While embankments substantially reduce the frequency of flooding, they also introduce residual flood risk associated with overtopping and structural failure during extreme hydrological events (Di Baldassarre et al., 2009; Apel et al., 2009; Merz et al., 2010). In embanked systems, flood hazard is therefore not solely governed by exceedance of channel conveyance capacity, but increasingly by the dynamics of levee failure mechanisms.

https://doi.org/10.5194/egusphere-2026-2992
Preprint. Discussion started: 24 June 2026

Overtopping-induced levee breaches result from complex interactions between hydraulic loading, soil erodibility, and progressive headcut migration (Wahl, 1998; Froehlich, 2008; Hanson and Cook, 2004). Once local bed shear stress exceeds critical resistance thresholds, erosion accelerates through positive hydraulic–morphodynamic feedback. Increasing discharge enhances erosion, which enlarges the breach opening and further increases flow, potentially leading to rapid inundation of the surrounding areas (ASCE/EWRI Task Committee on Dam/Levee Breaching, 2011; Morris et al., 2007).

Despite advances in numerical flood modelling, many operational hazard assessments still represent levee breaches using predefined geometries or empirical growth relationships (Wahl, 1998; Froehlich, 2008). While computationally efficient and suitable for probabilistic large-scale applications (Vorogushyn et al., 2009), such simplified approaches neglect the dynamic coupling between hydraulic forcing and erosion processes and typically assume independent breach scenarios.

Recent developments in two-dimensional (2D) hydrodynamic solvers have significantly improved the simulation of flow dynamics in low-gradient environments, where lateral spreading dominates longitudinal routing (Bates et al., 2010; Neal et al., 2012). High-resolution modelling has been shown to be crucial in flat terrains, where small elevation differences control large inundation patterns (Horritt and Bates, 2001). However, fully coupled hydrodynamic–morphodynamic simulations of levee breach evolution remain relatively underrepresented in event-based reconstructions, especially for real cases involving multiple simultaneous breaches.

The May 2023 extreme rainfall event in Emilia-Romagna represents one of the most severe hydrological crises in recent decades in Italy. Prolonged precipitation over already saturated catchments produced exceptional discharge peaks and widespread levee failures across several rivers. Along the Senio River, multiple breaches developed following overtopping, leading to rapid and extensive inundation of the surrounding areas.

Event-based reconstruction provides essential insight into physical flood processes and complements probabilistic flood risk approaches (Merz et al., 2010). In this context, physically based hydrodynamic–morphodynamic modelling offers a powerful framework for analysing residual flood risk mechanisms in embanked systems.

The objective of this study is to show that this modelling approach can reliably reproduce complex flood events characterized by multiple simultaneous levee breaches. To this end, the 16–19 May 2023 flood event along the Senio River is reconstructed using a high-resolution 2D modelling framework based on the parallel solver PARFLOOD (Vacondio et al., 2014; Vacondio et al., 2017), coupled with a morphodynamic model for levee erosion (Dazzi et al., 2019). The simulation is then used to analyse levee breach formation and evolution, quantify overflow volumes, inundation extent, water depth distribution, and flood arrival times, and to discuss the implications for residual flood risk in embanked river systems.

2 Study Area

The Senio River is a right-bank tributary of the Reno River located in the Emilia-Romagna region (Italy, Fig. 1a). In its lower reach, the river flows through a very low-gradient alluvial plain characterized by continuous artificial levees, intensive agricultural land use, drainage infrastructure, and scattered urban settlements, including the small towns of Castel Bolognese,

https://doi.org/10.5194/egusphere-2026-2992
Preprint. Discussion started: 24 June 2026

Solarolo and Cotignola. The territory is part of a highly engineered fluvial and reclamation system typical of the region, where artificial embankments play a fundamental role in flood containment; therefore, these areas are particularly sensitive to breach-driven flooding.

The geographical setting of the Senio River basin and the modeled river reach are shown in Fig. 1. The basin, closed at Castel Bolognese, has an area of 262.5 km² (Fig. 1b). The modeled reach (approximately 23 km) extends along the embanked lowland sector of the river and includes the three hydrometric stations of Tebano, Castel Bolognese, and Cotignola (Fig. 1c). It is worth noting that the drainage area between Tebano and Castel Bolognese is nearly the same, so that hydrological differences between the two sections are negligible.

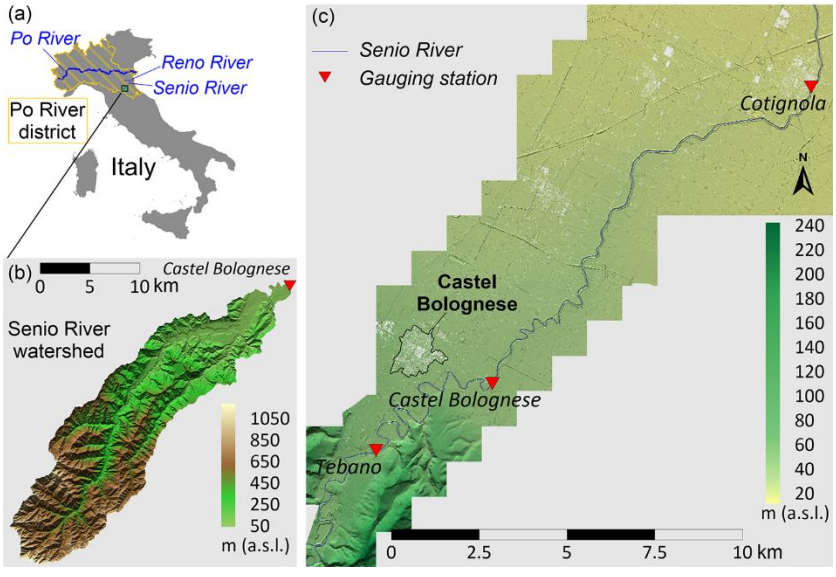

Figure 1: Study area. (a) Location of the Senio River basin within the Po River district, Northern Italy. (b) Senio River basin and drainage area closed at Castel Bolognese (262.5 km²), derived from the digital elevation model. (c) Modeled river reach (23 km) with hydrometric stations (Tebano, Castel Bolognese, Cotignola) and map of terrain elevations.

2.1 The May 2023 hydro-meteorological events

May 2023 was characterized by an unprecedented pluviometric anomaly over the Emilia-Romagna region. Two severe rainfall events affected the region between 1–3 May and 16–17 May 2023, respectively, both associated with a deep synoptic-scale trough over the central Mediterranean and a blocking anticyclonic ridge over eastern Europe. This large-scale configuration induced persistent cyclonic circulation and prolonged moisture advection toward northern Italy, favoring quasi-stationary precipitation systems over the central-eastern sector of the region (ARPAE Emilia-Romagna, 2023). In both events, intense precipitation resulted from the interaction between moist air masses advected from the southeastern Mediterranean and colder northeasterly flows, combined with low-level convergence over the Romagna area. Orographic enhancement (Stau effect)

https://doi.org/10.5194/egusphere-2026-2992
Preprint. Discussion started: 24 June 2026

along the Apennine relief further intensified rainfall over the windward slopes, particularly in the hilly and mountainous areas where the Senio basin is located.

Cumulative precipitation between 1 and 17 May reached exceptional values across the Senio basin. During the second event alone (16–17 May), six out of seven gauges exceeded their historical 24-hour rainfall records (ARPAE Emilia-Romagna, 2023). The spatial distribution of cumulative rainfall during the two main events is shown in Fig 2. The first event (1–3 May; Fig. 2a) produced widespread and intense precipitation over the central-eastern sector of the region, substantially contributing to basin-wide soil saturation. The second event (16–17 May; Fig. 2b) was characterized by particularly high accumulations over the Apennine foothills and the Senio basin, thereby intensifying runoff generation and producing extreme hydraulic conditions in the embanked lowland reach. Areal rainfall estimates over the Senio basin closed at Castel Bolognese provide a quantitative assessment of the magnitude of the event. Maximum daily areal rainfall values reached 123 mm and 153 mm during the first and second events, respectively, while two-day accumulations reached 169 mm and 207 mm. These values exceed previously recorded historical maxima for the basin, with records dating back to 1921. The total areal rainfall amounted to approximately 183 mm for the 1–3 May event and 210 mm for the 16–17 May event, corresponding to rainfall volumes of approximately 48 and 55 million cubic meters, respectively.

Statistical analysis of annual maxima for one- and two-day durations (1921–2021), based on the Generalized Extreme Value (GEV) distribution with L-moment parameter estimation (Hosking and Wallis, 1997), indicates return periods exceeding 500 years for the maximum daily and two-day rainfall depths associated with the May 2023 events (Regione Emilia-Romagna, 2023). These values substantially exceed the typical design return period adopted for hydraulic protection in the region (200 years), further confirming the exceptional magnitude of the hydro-meteorological forcing.

The extraordinary rainfall during the mid-May event, occurring over soil already saturated by the early-May event, generated extreme runoff in the upstream mountainous portion of the basin. The resulting flood wave propagated downstream toward the embanked lowland reach of the Senio River, where confinement by artificial levees caused water levels to approach levee crest, ultimately triggering overtopping and subsequent levee breaches. Conversely, during the 1–5 May event discharge levels were exceptionally high along the entire reach and only minor overtopping was reported.

While the main rainfall associated with the two events occurred between 1–3 May and 16–17 May 2023, water levels within the river channel remained elevated until 5 May and 19 May, respectively. For clarity, the two events are referred to as the 1–5 May and 16–19 May flood events. All times reported in this study refer to local standard time (UTC+1).

https://doi.org/10.5194/egusphere-2026-2992
Preprint. Discussion started: 24 June 2026

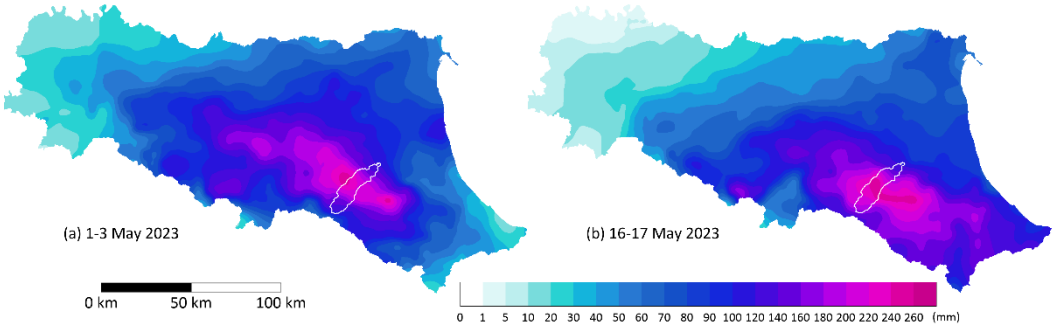

Figure 2: Spatial distribution of cumulative rainfall during the May 2023 events. (a) 1–3 May 2023; (b) 16–17 May 2023. Rainfall fields derived from the ERG5 dataset (ARPAE Emilia-Romagna, 2023). The outline of the Senio River basin is superimposed.

2.2 Hydrometric analysis

Hydrometric data from three gauging stations along the Senio River (Fig. 1c) - Tebano (upstream), Castel Bolognese (intermediate), and Cotignola (downstream) - were analyzed to characterize the hydraulic response of the river system and to support model calibration and validation. Observed stage hydrographs for the two flood events are shown in Fig. 3. During both the 1–5 May and the 16–19 May flood event, water levels exceeded maximum warning thresholds at all three stations.

At Tebano, the upstream station, water levels approached or locally exceeded levee crest elevation prior to breach initiation during the 16–19 May event. The formation of breaches both upstream and downstream of the station influenced stage evolution through breach-induced drawdown and redistribution of discharge, particularly during the peak and early recession phases of the flood wave.

At Castel Bolognese, peak water levels during the 16–19 May event exceeded historical reference values and were significantly higher than those recorded during the 1–5 May event; moreover, the mid-May hydrograph exhibits a complex evolution and a different behaviour compared to early-May. As shown in Fig. 3b, the rising limb of the hydrograph does not exhibit a particularly steep increase, as it was influenced by upstream floodplain inundation and early levee failures that partially attenuated and redistributed the incoming flood volume. Immediately after the peak time, a relatively rapid decrease in water level is observed, which can be associated with the progressive opening of levee breaches and the consequent diversion of flow toward the lowland areas outside the levee system. Subsequently, the recession limb shows a deviation from the typical exponential decay, visible as a local change in curvature of the hydrograph. As discussed in Section 3, this behaviour is consistent with the delayed re-entry of part of the flow from the external inundated areas back into the main channel.

At Cotignola, located in the low-gradient downstream reach, the flood wave exhibited attenuation of peak levels but prolonged high-water conditions due to floodplain storage and multiple levee failures along the reach.

https://doi.org/10.5194/egusphere-2026-2992
Preprint. Discussion started: 24 June 2026

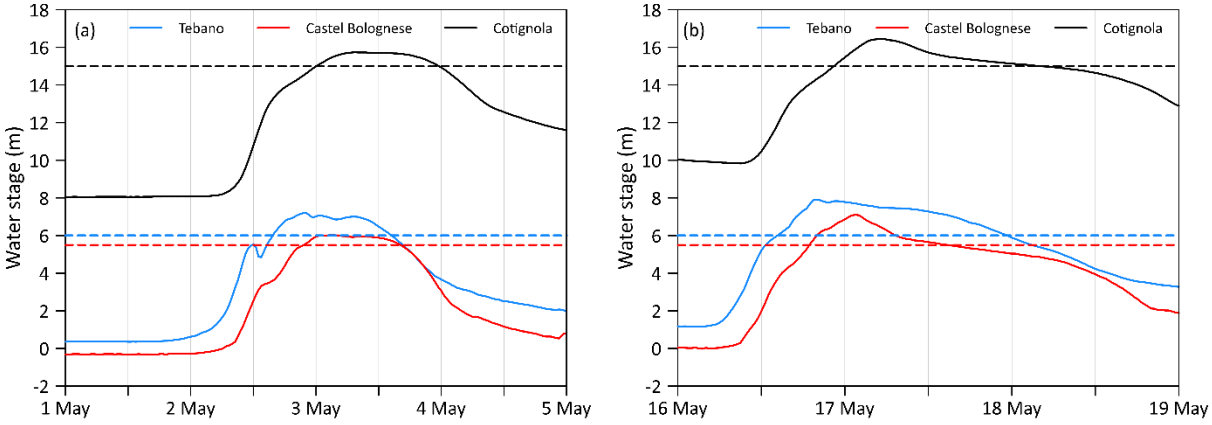

Figure 3: Observed stage hydrographs at Tebano, Castel Bolognese, and Cotignola during the May 2023 flood events. (a) 1–5 May flood event. (b) 16–19 May flood event. Dashed horizontal lines indicate the maximum warning threshold at each gauging station, with colors corresponding to the respective stage time series. The time axis refers to 00:00 of each day. The water stage is measured according to the gage reference level.

The observed exceedance of historical stage levels and alert thresholds confirms that the May 2023 events represent the most severe hydraulic stress recorded in the instrumental period for the Senio River. The combined analysis of the three stations provides a consistent picture of the spatial evolution of the flood wave along the river corridor. These hydrometric records constitute the primary reference dataset for the hydraulic calibration and validation procedures described in Section 3. In particular, the early May 2023 event was used for the calibration of channel roughness, while the mid-May 2023 event was simulated in detail to analyse levee breach formation and the resulting inundation of the areas outside the levee system along the left bank.

2.3 Availability of high-resolution topographic and observational data

An unusually favorable aspect of this event was the availability of high-quality and temporally consistent topographic datasets. A detailed LiDAR survey with a spatial resolution of 0.5 m, including coeval orthophotos with a ground sampling distance (GSD) of 15 cm, was conducted by the Emilia-Romagna Regional Authority in late March and early April 2023, approximately one month before the flood events. This dataset covered the entire study area, including all the areas outside the main channel that were affected by inundations in May. The availability of such recent pre-event topographic data significantly reduces uncertainty associated with terrain representation and is rarely available in post-event analyses. The dataset allowed accurate reconstruction of levee geometry prior to failure, precise representation of micro-topographic controls on flood propagation and inundation dynamics, and reliable identification of anthropogenic features influencing flow redistribution across the lowland areas.

It is well known that standard airborne LiDAR systems are unable to penetrate the water column. Although the pre-event survey was carried out under low-flow conditions, the submerged portion of the river channel was therefore not represented in the LiDAR-derived digital terrain model (DTM). Fortunately, for the 23 km river reach analyzed in this study, approximately

https://doi.org/10.5194/egusphere-2026-2992
Preprint. Discussion started: 24 June 2026

80 ground-surveyed cross-sections acquired in 2022 were available. These relatively recent field measurements were used to reconstruct the submerged channel geometry. The pre-event DTM was consequently corrected within the wetted channel areas, clearly identifiable in the coeval orthophotos, through an original anisotropic, cross-section-guided interpolation procedure. The approach is conceptually similar, though not identical, to the algorithm proposed by Song et al. (2020) for reconstructing river topography from surveyed cross-sections.

In addition, specific geometric corrections were applied to improve hydraulic consistency of the computational domain. Openings were introduced at road and railway embankments where culverts or underpasses were present but not properly resolved in the LiDAR-derived DTM. Crest elevations of thin retaining walls, not adequately represented despite the high spatial resolution, were locally corrected. Bridges were explicitly included in the hydrodynamic model as internal boundary conditions following the implementation described in Dazzi et al. (2020). The resulting corrected DTM was adopted as the reference topographic dataset for all subsequent hydrodynamic simulations.

A second LiDAR survey, also accompanied by coeval orthophotos, was conducted shortly after the mid-May flood event. Although spatially limited to the river corridor and a 250 m-wide buffer strip on both sides of the channel, this dataset was crucial for identifying the final position of levee breaches, measuring final breach widths, and assessing crest lowering and morphological changes. For instance, the breach located at “La Steccaia” was clearly identifiable in post-event orthophotos and LiDAR-derived elevation models (Fig. 4).

The comparison between pre- and post-event surveys enabled precise identification of the eroded section and quantitative assessment of the associated morphological change. The availability of pre-event and post-event high-resolution LiDAR datasets represents a major strength of the present study and provides an unusually robust basis for morphodynamic model calibration and validation.

2.4 Flood extent and impact data

For this flood event, the integration of hydrometric records, high-resolution pre- and post-event LiDAR data, official flood mapping, and eyewitness observations provides a comprehensive multi-source dataset for event-based hydrodynamic–morphodynamic reconstruction. Flood extent information was derived from official mapping conducted by Civil Protection authorities, surveys performed by the involved municipalities, and satellite-derived flood maps where available. These datasets provided a spatial reference framework for model validation. In addition, a series of eyewitness testimonies collected in the affected municipalities provided valuable qualitative and semi-quantitative information regarding flood arrival times and maximum water depths reached in residential areas. At some urban locations, observed maximum depths were documented with sufficient detail to allow direct comparison with simulated peak water levels.

https://doi.org/10.5194/egusphere-2026-2992
Preprint. Discussion started: 24 June 2026

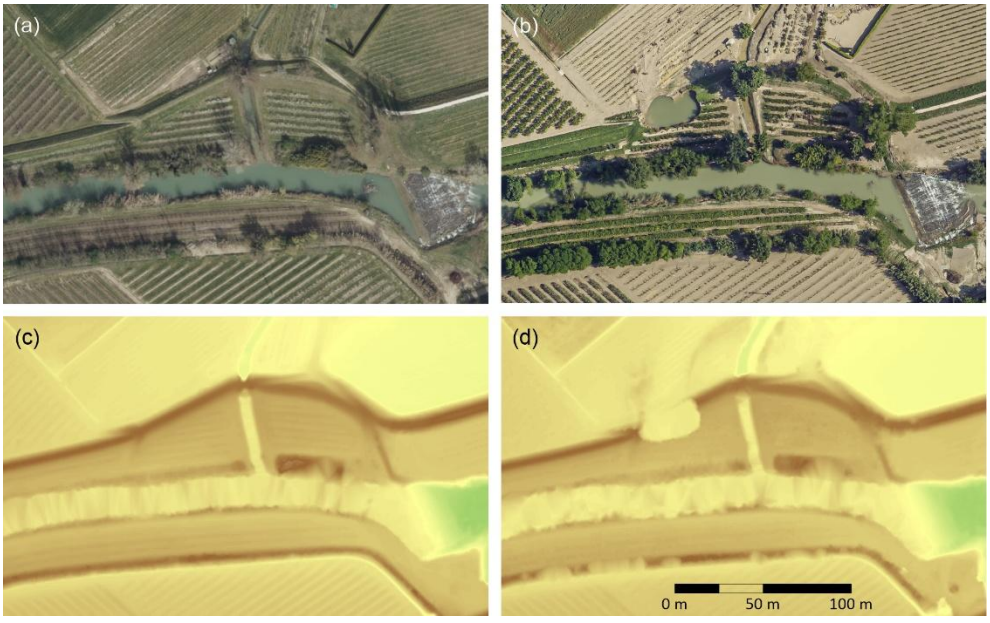

Figure 4: Morphological changes at the "La Steccaia" levee breach. (a) Pre-event orthophoto; (b) Post-event orthophoto (© Regione Emilia-Romagna Geoportal); (c) Pre-event DTM; (d) Post-event DTM. The comparison highlights the final breach width and crest lowering induced by the mid-May 2023 flood event.

3 Materials and Methods

3.1 Hydrodynamic model formulation

Flood propagation was simulated using the 2D model PARFLOOD, a parallel finite-volume solver (Vacondio et al., 2014; Vacondio et al., 2017) that solves the 2D depth-averaged shallow water equations (SWEs) in conservative integral form over each computational cell:

$$\frac{d}{dt}\int_A \mathbf{U}\, dA + \int_C \mathbf{H}\cdot\mathbf{n}\, dC = \int_A (\mathbf{S}_0 + \mathbf{S}_f)\, dA, \tag{1}$$

where A is the cell area, C its boundary, $\mathbf{n}$ the outward unit normal vector, $\mathbf{U}$ is the vector of conserved variables, $\mathbf{H}$ the flux tensor in the horizontal directions, and $\mathbf{S}_0$, $\mathbf{S}_f$ are the bed slope and friction source terms.

To guarantee preservation of steady states and ensure proper balance between flux gradients and topographic source terms, PARFLOOD adopts a formulation satisfying the so-called *C*-property (Rogers et al., 2003; Liang and Borthwick, 2009). In this approach, the fluxes are expressed in terms of the water surface elevation $\eta=h+z$, yielding:

$$\mathbf{U} = \begin{bmatrix} h \\ uh \\ vh \end{bmatrix}, \mathbf{F} = \begin{bmatrix} uh \\ u^2h + \frac{1}{2}g(h^2 - 2hz) \\ uvh \end{bmatrix}, \mathbf{G} = \begin{bmatrix} vh \\ uvh \\ v^2h + \frac{1}{2}g(h^2 - 2hz) \end{bmatrix}, \tag{2}$$

where h is the water depth, u and v are the velocity components in the x and y directions, z is the bed elevation, and g is the gravitational acceleration.

https://doi.org/10.5194/egusphere-2026-2992
Preprint. Discussion started: 24 June 2026

The source terms are given by:

$$\mathbf{S}_0 = \begin{bmatrix} 0 \\ -gh\frac{\partial z}{\partial x} \\ -gh\frac{\partial z}{\partial y} \end{bmatrix}, \mathbf{S}_f = \begin{bmatrix} 0 \\ -gh\frac{n^2 u\sqrt{u^2+v^2}}{h^{4/3}} \\ -gh\frac{n^2 v\sqrt{u^2+v^2}}{h^{4/3}} \end{bmatrix}, \quad (3)$$

where n is Manning's roughness coefficient.

The equations are discretized on a Cartesian grid using a Finite Volume scheme with an HLLC approximate Riemann solver (Toro, 1999). Details of the numerical discretization, time integration, and wetting–drying treatment are reported in Vacondio et al. (2014, 2017). The solver is fully parallelized and optimized for GPU architectures, enabling efficient simulation of very large computational domains. Internal hydraulic structures such as bridges are represented through internal boundary conditions following Dazzi et al. (2020).

High-resolution topography is critical in flat floodplains (Horritt and Bates, 2001). Although PARFLOOD is capable of handling multi-resolution grids (Vacondio et al., 2017), the computational domain in the present study was discretized using a uniform 1 m resolution grid derived from the 0.5 m pre-event LiDAR survey. This choice, while increasing computational demand, was deliberately adopted to fully exploit the high-resolution digital terrain model across the entire domain, including the floodable areas outside the main river channel and the urban centers. The high-resolution DTM was resampled to the computational grid while preserving levee crest elevations and embankment geometry through elevation-constrained interpolation techniques, thus avoiding artificial smoothing of hydraulically critical features. The final grid consisted of approximately 100 million computational cells, allowing detailed representation of levee geometry and floodplain micro-topography.

This uniform discretization also ensures numerical consistency in the representation of morphodynamic processes and avoids resolution transitions in proximity of levee crests and breach locations, where accurate coupling between hydraulic forcing and erosion dynamics is essential.

3.2 Morphodynamic model for breach erosion and bank failure

Levee breach evolution is simulated by restricting bed elevation changes to predefined erodible levee zones, where potential breaches may occur. Within these areas, bottom elevation is updated according to (Dazzi et al., 2019):

$$\frac{\partial z}{\partial t} = -\frac{E}{1-p}, \quad (4)$$

where p is bed porosity and E is the erosion rate (volume eroded per unit area and time). Erosion is computed using a linear excess shear stress formulation (Partheniades, 1965; Hanson and Simon, 2001):

$$E = \max\left(0, k_d(\tau - \tau_c)\right), \quad (5)$$

https://doi.org/10.5194/egusphere-2026-2992
Preprint. Discussion started: 24 June 2026

where k_d is the erodibility coefficient, τ is the bed shear stress, and τ_c is the critical shear stress for sediment motion. The shear stress is evaluated consistently with the hydraulic solution through the Manning-based formulation.

This approach allows erosion to develop dynamically as soon as overtopping generates shear stress exceeding the critical value. The breach geometry is not predefined: breach opening, deepening, and lateral expansion emerge automatically from the coupling between hydraulic forcing and erosion response.

Only erosion (scour) is considered, while deposition is neglected under the assumption that eroded material is rapidly transported away by the high-energy overtopping flow. Water mass conservation is ensured by adjusting the local free-surface elevation after each erosion update so that the water volume within each cell is preserved.

The morphodynamic response is strongly controlled by the erodibility parameters τ_c and, especially, k_d. Their values are known to exhibit significant variability, often spanning several orders of magnitude depending on soil texture, plasticity, compaction, and water content (Hanson and Hunt, 2007; Fell et al., 2013). Although laboratory methods such as the Jet Erosion Test exist (Hanson and Cook, 2004), parameter uncertainty remains substantial. Empirical relationships between k_d and τ_c (Hanson & Simon, 2001; Nguyen et al., 2017) and soil-based estimation formulas (Wu, 2013) provide guidance when direct measurements are unavailable.

In addition to vertical erosion, breach enlargement is influenced by lateral bank collapse. As the breach deepens, adjacent slopes may become unstable and fail gravitationally. To account for this mechanism, a bank failure algorithm based on slope threshold criteria was implemented following Guan et al. (2014), adapted for GPU execution. For each cell, local slopes toward neighboring cells are computed. If the absolute slope exceeds a prescribed critical angle (different values are used for wet and dry cells), the bed elevation is locally adjusted to reduce the slope toward a stable deposition angle. Equal and opposite corrections are applied to neighboring cells, ensuring conservation of sediment mass. This correction procedure is iterated until no unstable slopes remain. To reduce computational cost, slope stability checks are not performed at every hydraulic time step but at a larger interval, without affecting the final breach geometry.

The combined effect of shear-driven erosion and slope-driven bank failure allows the model to reproduce both breach deepening and widening processes in a physically consistent manner, without prescribing breach dimensions a priori, consistent with conceptual breach models described by the ASCE/EWRI Task Committee on Dam/Levee Breaching (2011).

3.3 Calibration of hydraulic roughness in the river channel

River roughness calibration was performed using the severe1-5 May 2023 event, which provides an ideal condition for calibration. The river corridor was schematized into two hydraulically homogeneous zones within the channel–floodplain system: (1) the incised main channel and (2) the overbank areas. This simplified parametrization was deliberately adopted in order to limit parameter equifinality, while maintaining the physical interpretability of calibrated parameters. Rather than assigning Manning's roughness coefficients directly from literature tables, a trial-and-error procedure was adopted. Observed water level hydrographs at the upstream station of Tebano and the downstream station of Cotignola were imposed as time-varying boundary conditions in the hydrodynamic simulation. The Manning coefficients associated with the two zones were

https://doi.org/10.5194/egusphere-2026-2992
Preprint. Discussion started: 24 June 2026

varied within physically reasonable ranges derived from hydraulic literature and regional experience, constraining the channel to be smoother than the floodplain. For each parameter combination, the simulated water level hydrograph at the intermediate station of Castel Bolognese was extracted and compared with recorded levels. Particular attention was paid to the reproduction of peak water levels, to the overall hydrograph shape, and especially to the phase alignment between simulated and observed water levels, which are highly sensitive to hydraulic resistance parametrization in low-gradient rivers (Moramarco et al., 2005; Aricò et al., 2009; Barbetta et al., 2012).

Figure 5a shows the comparison between simulated and observed water levels at the Castel Bolognese gauging station for the final calibrated parameter set. Quantitatively, this configuration yields a peak water level overestimation of only 0.08 m, a root mean square error (RMSE) of 0.29 m over the event duration, and a time shift of about □1 hour. Although a perfect phase match is not achieved, the reconstructed hydrograph satisfactorily captures the rising limb, peak stage, and recession trend of the recorded levels. A minor secondary rise observed in the recession limb is likely associated with delayed inflow from a small tributary entering the river upstream of Castel Bolognese, which is not explicitly represented in the model.

In addition, the calibrated roughness reliability is confirmed by the comparison between reconstructed and measured discharges at Tebano during the 1–5 May event (Fig. 5b). Although only two discharge measurements are available, and both refer to the recession limb of the hydrograph, the simulated values are in good agreement with the observations.

The final calibrated Manning roughness coefficients are equal to 0.058 s $m^{-1/3}$ for the incised main channel and 0.10 s $m^{-1/3}$ for the overbank areas. These values, although on the higher side, fall within the range reported in the hydraulic literature for natural alluvial channels and highly vegetated overbank areas (e.g., Chow, 1959; Arcement and Schneider, 1989), as is the case in the present study. By performing calibration under near-overtopping but non-breaching conditions, channel resistance parameters were constrained independently of morphodynamic effects. This approach ensures that subsequent simulations of levee breach evolution during the 16–19 May event are not influenced by artificial compensation between hydraulic roughness and erosion parameters.

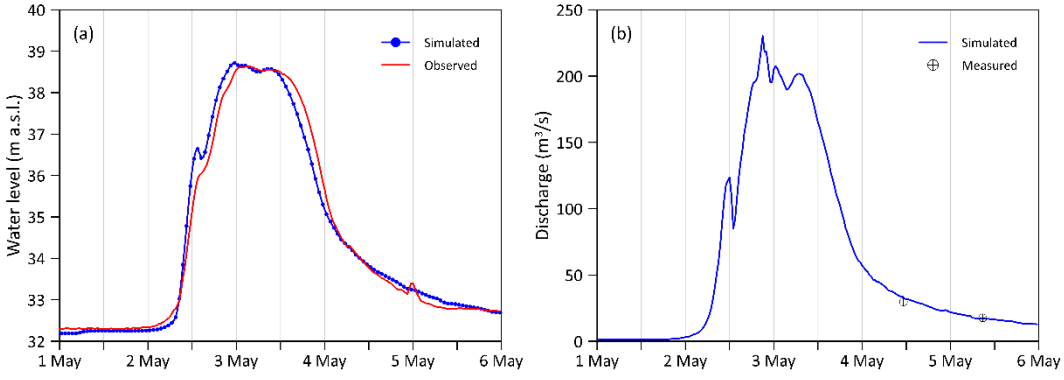

Figure 5: Comparison between observed and simulated data used for roughness calibration during the 1–5 May 2023 flood event. (a) Water levels at the Castel Bolognese gauging station. (b) Reconstructed discharges at the Tebano gauging station compared with available discharge measurements.

https://doi.org/10.5194/egusphere-2026-2992
Preprint. Discussion started: 24 June 2026

3.4 Floodplain roughness parametrization and urban treatment

Roughness values outside the levee system were assigned based on land-use classification derived from CORINE land cover maps available for the Emilia-Romagna Region. Following the approach proposed by Papaioannou et al. (2018), and considering the third-level CORINE classification, land use was initially grouped into 25 categories, each associated with a representative Manning's roughness coefficient (see Table 1 in Papaioannou et al., 2018). Considering that some CORINE classes were not present in the study area, that channel roughness was independently calibrated (Section 3.3), and that several classes share similar roughness values, the classification was simplified into nine representative roughness categories. The corresponding Manning coefficients and associated land-use classes are reported in Table 1, while the final roughness map with their spatial distribution over the floodable areas is shown in Fig. A1 of Appendix A.

Urban areas were treated using the "building hole" technique (Schubert and Sanders, 2012). Building footprints were superimposed onto the DTM and locally removed from the computational domain, so that water cannot enter building cells and flow is explicitly resolved within streets and open spaces. The adoption of this approach was made possible by the high spatial resolution of the computational grid (1 m), which allows explicit geometric representation of individual buildings. The building-hole representation can be regarded as a conservative assumption when evaluating maximum water levels along streets, since it neglects potential storage within buildings. In some cases, allowing water to enter buildings may reduce water levels locally due to additional storage capacity.

The consistency of the adopted floodplain roughness values was indirectly evaluated through comparison between simulated and observed flood arrival times at selected locations within the inundated area. Since flood propagation speed in low-gradient plains is strongly influenced by surface resistance, agreement between simulated and reported arrival times provides additional support for the adequacy of the selected roughness parametrization.

Table 1 – Manning's roughness coefficients assigned to areas outside the levee system based on aggregated CORINE land-use classes adopted in this study.

Land use categories	CORINE classification (level 3, grouped)	Manning's *n* ($s \cdot m^{-1/3}$)
Artificial surfaces (Urban fabric, Industrial commercial and transport units, Mine, dump and construction sites)	1.1.1,1.1.2,1.2.1,1.2.4, 1.3.1.,1.3.2,1.3.3	0.013
Artificial surfaces (Artificial, non-agricultural vegetated areas)	1.4.1.,1.4.2	0.025
Agricultural areas (Arable land)	2.1.1, 2.1.2	0.030
Agricultural areas (Permanent crops)	2.2.1, 2.2.2, 2.2.3	0.080
Agricultural areas (Pastures)	2.3.1	0.035
Agricultural areas (Heterogeneous)	2.4.1, 2.4.2	0.040
Agricultural areas (with significant natural and sclerophyllous vegetation)	2.4.3, 3.2.3	0.050
Forests and semi natural areas (Broad-leaved forests)	3.1.1	0.100
Forests and semi natural areas (Sparsely vegetated areas)	3.3.3	0.027

https://doi.org/10.5194/egusphere-2026-2992
Preprint. Discussion started: 24 June 2026

3.5 Selection and constrained calibration of morphodynamic parameters

Direct geotechnical measurements of levee materials were not available for the study reach. Even when soil properties are known, deriving reliable morphodynamic parameters for breach modelling remains challenging. While empirical formulations exist for estimating the critical shear stress τ_c from soil characteristics (e.g., Chang et al., 2011), the erodibility coefficient k_d which controls erosion rates in excess shear stress formulations - cannot be robustly inferred from standard geotechnical parameters and exhibits large variability in experimental datasets (Hanson et al., 2010). Indeed, experimental values of k_d and τ_c reported in the literature show a very large scatter, even for materials with similar properties. The distribution of these experimental data, together with the empirical trend proposed by Hanson and Simon (2001), is illustrated in Fig. 6.

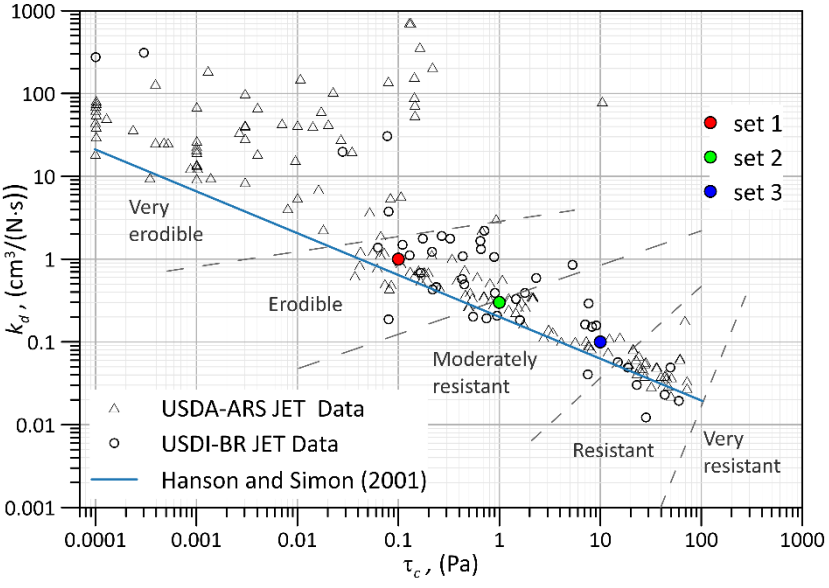

Figure 6: Experimental values of critical shear stress (τ_c) and erodibility coefficient (k_d) for cohesive materials (adapted from Hanson et al., 2010), together with the empirical relationship proposed by Hanson and Simon (2001). The parameter sets adopted in this study (sets 1–3) are also shown.

In the absence of site-specific erosion tests and time-resolved observations of breach evolution, a constrained parameter selection strategy was adopted. A single pair of morphodynamic parameters (τ_c, k_d) was assumed for all ten documented breaches, reflecting the overall homogeneity of embankment materials and the lack of detailed spatial characterization. Three candidate parameter pairs (sets 1–3 in Fig. 6 and Table 2) were selected within the experimentally observed ranges for cohesive soils reported by Hanson et al. (2010), considering the empirical relationship between τ_c and k_d discussed in the literature. Parameter selection was primarily constrained by the ability of the model to reproduce the observed stage hydrograph at Castel Bolognese, which is strongly influenced by upstream breach formation and evolution. In addition, parameter sets were evaluated through comparison between simulated and observed post-event breach geometries, focusing on final breach width and overall breach shape. Emphasis was placed on the “La Steccaia” breach, for which high-resolution topographic data

https://doi.org/10.5194/egusphere-2026-2992
Preprint. Discussion started: 24 June 2026

allowed detailed geometric assessment. Among the tested combinations, parameter set 2 yielded the best reproduction of the recorded water levels at Castel Bolognese and also provided the best agreement with the observed final breach dimensions.

Table 2 – Tested morphodynamic parameter sets

Set	τ_c (Pa)	k_d (cm³/(N s))
1	0.1	1.0
2	1.0	0.3
3	10.0	0.1

Hydraulic consistency was used as an additional criterion. Excessively high k_d values produced unrealistically rapid erosion and premature stage drawdown, whereas overly resistant parameter sets failed to reproduce observed breach widening. Under the extreme overtopping conditions of the event, computed shear stresses largely exceeded τ_c. Consequently, model results were more sensitive to variations in k_d than to moderate changes in τ_c.

The final parameter set was therefore selected to ensure both morphodynamic realism and hydraulic coherence. Porosity p and the characteristic slope angles adopted in the bank failure algorithm φ_{wet}, φ_{dry} and φ_{dep} were kept constant and equal to 0.4, 31°, 50° and 27°, respectively.

3.6 Performance metrics for flood extent evaluation

Standard spatial performance metrics were used to evaluate the agreement between simulated and observed flood extent, following approaches commonly adopted in flood inundation modelling (e.g., Bates and De Roo, 2000; Aronica et al., 2002; Pappenberger et al., 2005; Di Baldassarre and Montanari, 2009; Tavares da Costa et al., 2019; Deiana et al., 2023). Each computational cell was classified as flooded or non-flooded according to both the simulated results and the reference map derived from Civil Protection data. Based on this comparison, the domain was partitioned into four classes: true positives (TP), corresponding to correctly predicted flooded cells; false positives (FP), representing overestimated flooded areas; false negatives (FN), indicating missed flooded areas; and true negatives (TN), corresponding to correctly identified non-flooded cells. The overall agreement between simulated and observed flood extent was quantified using the Jaccard index (J), also known as the Critical Success Index (CSI), defined as:

$$J = \frac{A_{sim} \cap A_{obs}}{A_{sim} \cup A_{obs}} = \frac{TP}{TP+FP+FN}, \quad (6)$$

where A_{sim} and A_{obs} represent the simulated and observed flooded areas, respectively. The index ranges between 0 and 1, with values closer to 1 indicating better agreement between simulated and observed inundation patterns.

To further analyse model performance, additional indicators were computed, including the true positive rate (TPR) and the false positive rate (FPR), defined as:

$$TPR = \frac{TP}{TP+FN}, \; FPR = \frac{FP}{FP+TN}, \quad (7)$$

https://doi.org/10.5194/egusphere-2026-2992
Preprint. Discussion started: 24 June 2026

The TPR represents the fraction of observed flooded areas correctly identified by the model, while the FPR quantifies the proportion of non-flooded areas incorrectly classified as flooded. Both indices range between 0 and 1. Higher values of TPR (closer to 1) indicate better detection of flooded areas, whereas lower values of FPR (closer to 0) indicate fewer false alarms. Together, these metrics provide complementary information to the Jaccard index, allowing discrimination between underestimation and overestimation of flooded areas.

It should be noted that the definition of the comparison domain may influence the TN values. In the present study, the evaluation domain was limited to the modelled area, ensuring consistency between simulated and observed datasets.

In addition, the available point-based observations of maximum water depth were used to complement the spatial performance metrics, allowing validation of inundation intensity.

4 Results

The location of the levee breaches that occurred during the 16–19 May 2023 event is shown in Fig. 7, together with the control sections used to evaluate flow volumes and propagation dynamics. A total of ten breaches were documented along the modeled reach, exhibiting different hydraulic behaviours and spatial extents. This spatial framework provides the reference for the interpretation of the hydrodynamic and morphodynamic processes discussed in the following sections.

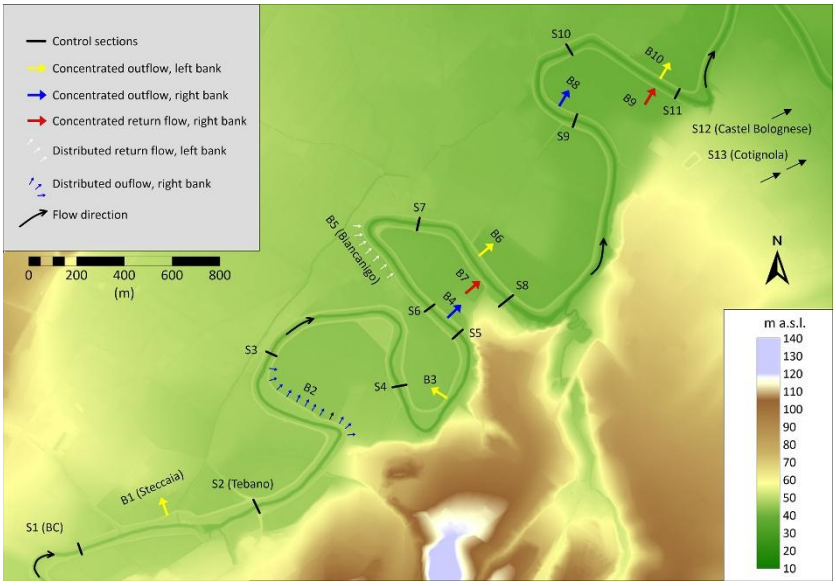

Figure 7: Location of levee breaches along the modeled reach of the Senio River during the 16–19 May 2023 flood event. Breaches are classified according to their position (left/right bank), hydraulic role (outflow or return flow), and spatial extent. Control sections used for discharge and volume analysis are also indicated.

https://doi.org/10.5194/egusphere-2026-2992
Preprint. Discussion started: 24 June 2026

4.1 Reconstruction of the flood wave along the river channel

The reconstruction of the flood wave along the Senio River was carried out within the same hydrodynamic–morphodynamic simulation used to reproduce levee breach evolution. Because breach formation directly affects water levels and discharges along the river, the inflow hydrograph and the evolution of breaches were determined consistently within the same modelling framework.

As described in Section 3, the upstream boundary condition was shifted to a section located upstream of the Tebano gauging station (S1 in Fig.7) in order to include the breach occurring at "La Steccaia" within the computational domain. Since neither water level nor discharge measurements were available at this location, the inflow hydrograph had to be reconstructed through an iterative procedure aimed at reproducing the observed water levels at Tebano (S2) while accounting for the influence of breach B1 and other downstream breaches.

Figure 8 shows the reconstructed inflow hydrograph together with the simulated discharges along the river reach obtained with the selected parameter set (set 2). A consistency check based on event-scale water volumes further supports the upstream boundary condition: the total volume under the hydrograph (51.3×10^6 m³) includes a non-negligible baseflow contribution, estimated at about 2.3×10^6 m³ and associated with the recession of the 1–5 May flood event. After removing this component, the effective runoff volume is approximately 49×10^6 m³, which is consistent with the estimated rainfall volume over the basin (about 55.1×10^6 m³). The resulting runoff coefficient is 0.89, which seems reasonable given the nearly saturated soil conditions preceding the event.

Figure 8 also illustrates the progressive discharge reduction between the upstream boundary section (S1), Tebano (S2), and Castel Bolognese (S12), reflecting the cumulative effects of outflows through levee breaches.

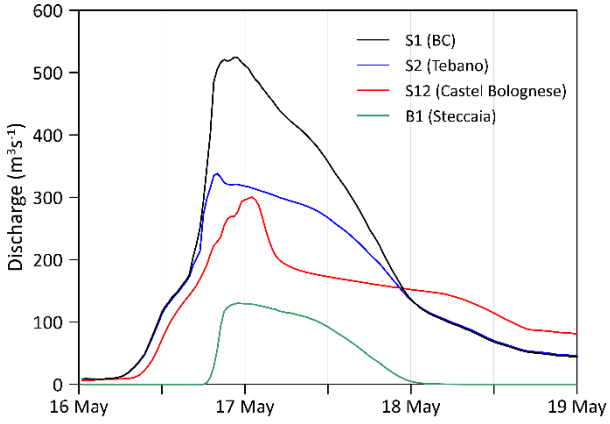

Figure 8: Reconstructed inflow hydrograph at the upstream boundary and simulated discharges along the Senio River reach during the 16–19 May 2023 flood event (time UTC+1). The figure shows the reconstructed inflow hydrograph, the simulated discharges at the Tebano and Castel Bolognese gauging stations, and the discharge flowing through the "La Steccaia" breach (B1), obtained with the selected morphodynamic parameter set (set 2).

https://doi.org/10.5194/egusphere-2026-2992
Preprint. Discussion started: 24 June 2026

In the same figure, the discharge flowing through the "La Steccaia" breach (B1) is also reported. This breach was the main responsible for the inundation of the areas on the left bank. Results obtained with the other tested parameter sets are reported in Appendix A (Fig. A2), highlighting the sensitivity of the simulated discharges to the adopted morphodynamic parameters, particularly along the reach between Tebano and Castel Bolognese.

The comparison between observed and simulated water levels at the Tebano gauging station (S2) is shown in Fig. 9a for the selected parameter set (set 2). Since the upstream boundary condition was derived through an inverse procedure aimed at reproducing the observed stage at Tebano, a close agreement between simulated and observed water levels is expected. The comparison therefore provides a consistency check of the reconstructed inflow hydrograph, confirming that the adopted procedure yields a realistic representation of the upstream hydraulic forcing.

Figure 9b presents the comparison between observed and simulated water levels at the Castel Bolognese gauging station (S12) for the three tested morphodynamic parameter sets. Significant differences among simulations are observed, reflecting the sensitivity of the hydrograph to the adopted erosion parameters. In particular, the timing and magnitude of the peak stage, as well as the subsequent evolution of the hydrograph, vary substantially among parameter sets.

Among the tested configurations, parameter set 2 provides the most convincing overall reproduction of the observed hydrograph. Although set 1 yields a slightly lower RMSE when the full event duration is considered (Table 3), set 2 better reproduces the timing and shape of the main phase of the event, including the peak stage and the subsequent rapid drawdown associated with breach development (see Fig. 9b). The simulation with set 2 reproduces the rising limb, peak stage, and most of the recession trend of the hydrograph with good accuracy. In addition, the simulation captures the rapid drop in water levels immediately after the peak, which is associated with the progressive opening of levee breaches and the consequent diversion of flow toward the inundated areas outside the levee system. The subsequent departure from the typical exponential decay of the recession limb, visible as a local change in curvature, is also reproduced.

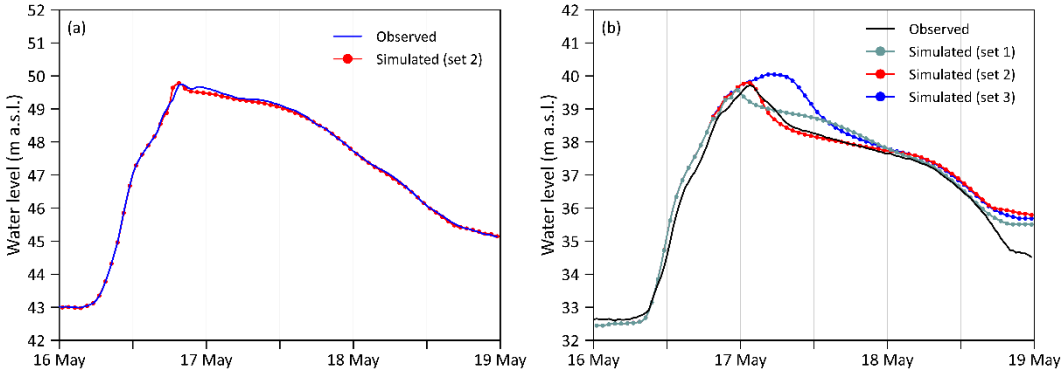

Figure 9: Comparison between observed and simulated water levels at the Tebano and Castel Bolognese gauging stations during the 16–19 May 2023 flood event. (a) Tebano gauging station (morphodynamic parameter set 2). (b) Castel Bolognese gauging station (comparison among the results obtained through all the morphodynamic parameter sets adopted).

https://doi.org/10.5194/egusphere-2026-2992
Preprint. Discussion started: 24 June 2026

However, a slight discrepancy is observed in the final part of the recession limb, which is not fully captured with any of the tested parameter sets. This behaviour may be related to residual uncertainties in the representation of breach geometry and their temporal evolution, which continue to influence flow redistribution during the later phase of the event. As shown in Table 3, excluding the final 12 hours of the event leads to a noticeable improvement in all performance metrics, with parameter set 2 providing the best results, confirming the good agreement between simulated and observed hydrographs during the main phase of the event.

It is worth emphasizing that the analysed event is characterized by the simultaneous occurrence of multiple levee breaches, which strongly alter the hydraulic response along the river reach. Under such conditions, the reproduction of water levels cannot be interpreted as a simple flood wave propagation problem, and the overall level of agreement obtained can therefore be considered more than satisfactory.

Overall, these results confirm that the reconstructed inflow hydrograph and the adopted model configuration provide a consistent representation of flood wave propagation along the river channel, while accounting for the complex hydraulic effects induced by multiple levee breaches and interactions between the river channel and the surrounding inundated areas.

Table 3 – Performance metrics (RMSE, MAE, and bias) computed for the three tested parameter sets (set 1, 2 and 3) at the Castel Bolognese gauging station. Metrics are evaluated over the full event duration (16-19 May 2023) and excluding the final 12 hours, during which all simulations tend to overestimate observed water levels.

Metric	Full event			Excluding last 12 h		
	set 1	set 2	set 3	set 1	set 2	set 3
RMSE (m)	0.37	0.42	0.57	0.31	0.24	0.51
MAE (m)	0.29	0.29	0.44	0.26	0.19	0.39
bias (m)	0.46	0.45	0.63	0.40	0.29	0.59

The simulated hydrographs show that the longitudinal evolution of flow along the river is not always characterized by a monotonic decrease in peak discharge and by the approximate conservation of flow volume, as would typically occur during flood wave propagation in the absence of lateral exchanges. In particular, at the Biancanigo breach (B5 in Fig. 7), part of the water previously spilled into the inundated areas outside the levee system returns to the river channel, resulting in higher discharge and volume downstream of the breach (S7) than upstream (S6) during part of the event (Fig. 10). The simulated discharge evolution at additional cross sections is reported in Appendix A (Fig. A3), where the combined effects of outflows and return flows along the modeled reach can be observed. Overall, this behaviour highlights the complex hydraulic interaction between the river channel and the inundated areas outside the levee system.

https://doi.org/10.5194/egusphere-2026-2992
Preprint. Discussion started: 24 June 2026

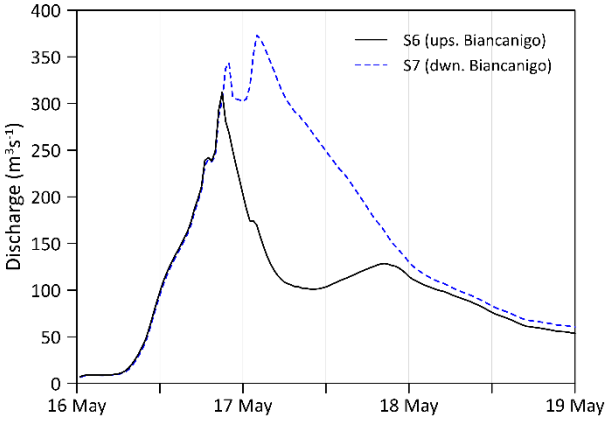

Figure 10: Comparison between observed and simulated water levels at the Tebano and Castel Bolognese gauging stations during the 16–19 May 2023 flood event. (a) Tebano gauging station (morphodynamic parameter set 2). (b) Castel Bolognese gauging station (comparison among the results obtained through all the morphodynamic parameter sets adopted).

4.2 Levee breach development

As shown in Fig. 7, a total of ten breaches (B1…B10) were documented along the modeled reach. They can be classified according to three main characteristics: (i) their position along the left or right bank, (ii) the hydraulic role of the breach (outflow or return flow), and (iii) the spatial extent of erosion along the levee. Breaches located along the right bank mainly caused inundation of areas that are hydraulically confined and would behave like natural floodplain zones in the absence of levees. In contrast, breaches located along the left bank allowed water to spread toward the surrounding lowland areas and contributed to the inundation of the towns of Castel Bolognese and Solarolo, together with other settlements located further downstream. From a morphological perspective, two main types of breach behaviour were observed. Some breaches developed as localized failures, where erosion affected a limited portion of the levee. Others evolved as distributed overtopping failures, where long sections of the levee crest were overtopped and progressively eroded.

Table 4 reports the flow volumes computed at the control sections shown in Fig. 7, together with the volume differences between consecutive sections. Negative differences indicate flow losses along the river reach, which can be attributed to outflows through levee breaches or temporary storage within the channel and adjacent areas. Conversely, positive differences represent net inflows or return flows occurring along the same reach. The values reported in Table 4 highlight the dominant role of breaches B1 (La Steccaia) and B2, which are associated with the largest flow losses. It should be noted, however, that breach B2 corresponds to a distributed failure along the right bank (Fig. 7), for which a downstream return flow is expected. In contrast, breach B5 (Biancanigo), representing a distributed return-flow breach, stands out for the significant volumes re-entering the main channel.

Due to space limitations, only two representative breaches are discussed in detail in the following: a localized outflow breach (La Steccaia) and a distributed return-flow breach (Biancanigo).

https://doi.org/10.5194/egusphere-2026-2992
Preprint. Discussion started: 24 June 2026

Table 4 – Cumulative flow volumes computed at selected control sections along the Senio River during the 16–19 May 2023 flood event, and corresponding volume differences between consecutive sections. Negative values indicate flow losses due to levee breaches or temporary storage within the channel and adjacent areas, while positive values represent flow gains associated with return flows or release of previously stored water.

Section n.	Breach n.	V (10^6 m^3)	ΔV (10^6 m^3)
S1 (Upstream boundary condition)	B1 (Steccaia)	51.3	-11.3
S2 (Tebano gauging station)	B2	40.1	-12.6
S3		27.5	+2.1
S4	B3	29.6	+7.3
S5	B4	37.0	-9.8
S6	B5 (Biancanigo)	27.1	+12.1
S7	B6, B7	39.2	-1.9
S8		37.4	-1.0
S9	B8	36.4	-3.4
S10	B9, B10	33.0	+1.2
S11		34.2	+0.8
S12 (Castel Bolognese)		35.0	-1.0
S13 (Cotignola)		34.0	

4.2.1 Localized outflow breach: La Steccaia

A representative example of a localized breach is the failure that occurred at La Steccaia (B1), whose simulated evolution is illustrated in Fig. 11. According to the simulation, overtopping started at around 18:00 on 16 May 2023, triggering progressive erosion of the levee crest. The breach deepened rapidly and reached its maximum depth approximately 5.5 hours later (23:30 on 16 May). The figure also shows the velocity field associated with the overtopping flow, highlighting the strong concentration of velocities near the developing breach. A more detailed view of the velocity field through the breach is provided in Fig. A4 in Appendix A and highlights the fine spatial resolution of the simulation, based on a computational grid with a spacing of 1 × 1 m.

Although the exact temporal evolution of the breach cannot be verified due to the lack of direct observations, the simulated timing is indirectly supported by the reported arrival times of the flood wave in the surrounding flooded areas, as discussed in the following section.

https://doi.org/10.5194/egusphere-2026-2992
Preprint. Discussion started: 24 June 2026

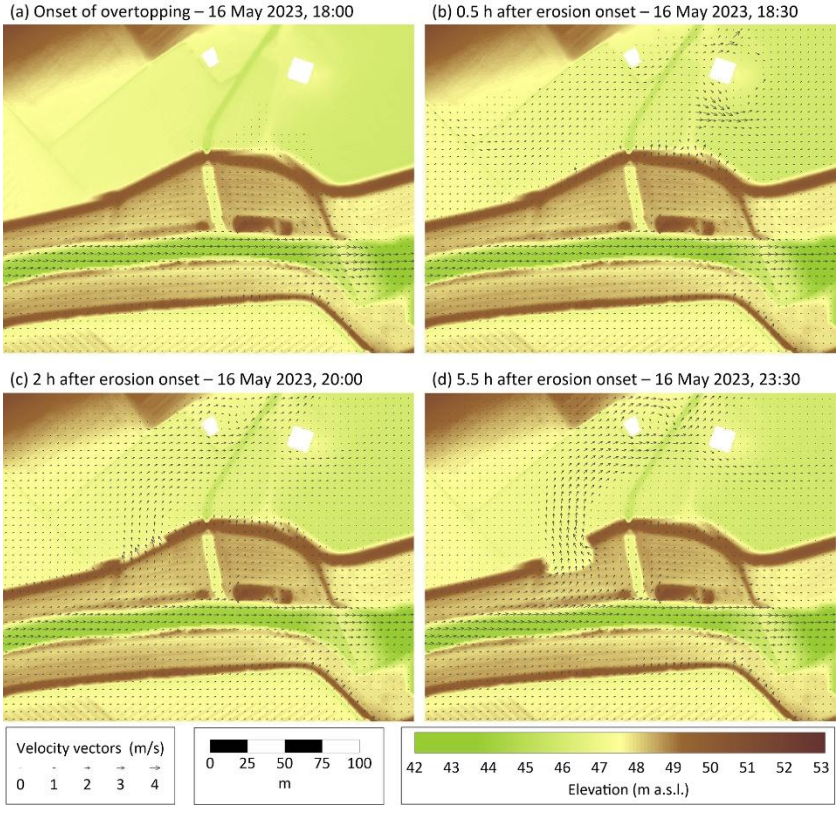

Figure 11: Temporal evolution of the La Steccaia levee breach during the 16–19 May 2023 flood event. The figure shows the progressive erosion of the levee together with the associated velocity field at selected times. Velocity vectors are represented every five cells in both directions for clarity.

505 The final geometry of the Steccaia breach can be compared with the post-event topographic data shown in Fig. 4d, but a direct comparison is also reported in Fig. 12. The cross-section derived from the simulation shows a very good agreement with the geometry obtained from the post-event DTM. Minor differences are observed in the slope of the breach sides, which appear slightly steeper in the post-event survey than in the simulated profile. Although this discrepancy could potentially be reduced by adjusting the morphological parameters controlling bank collapse, the overall reconstruction of the breach geometry is 510 already very satisfactory.

It is also worth noting that small elevation differences between the pre-event and post-event DTMs on the order of 10 cm are observed even outside the breached section. These differences are consistent with the expected accuracy of LiDAR-derived terrain models and may reflect both systematic offsets and local discrepancies. Such uncertainties may influence the representation of levee geometry and are further discussed in Section 5.

https://doi.org/10.5194/egusphere-2026-2992
Preprint. Discussion started: 24 June 2026

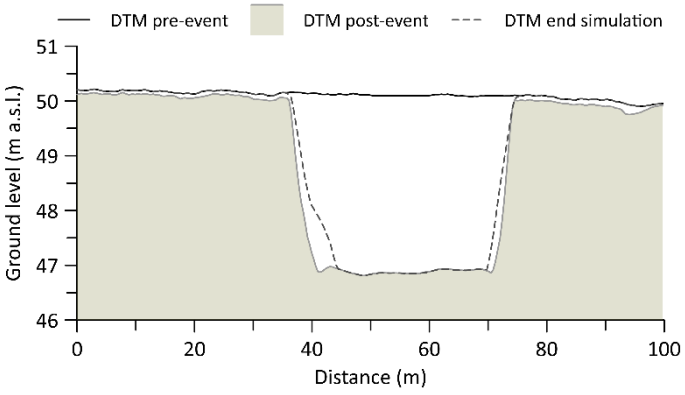

Figure 12: Comparison between simulated and observed cross-section at the La Steccaia levee breach. The observed profile is derived from the post-event LiDAR-based DTM, while the simulated profile corresponds to the final state of the morphodynamic modelling.

4.2.2 Distributed return-flow breach: Biancanigo

A representative example of a distributed breach with return flow is the failure that occurred at Biancanigo (B5), whose simulated evolution is shown in Fig. 13. The velocity field clearly indicates that part of the flow previously spilled onto the inundated areas outside the levee system re-enters the main channel at this location. In particular, water that exited the river at the Steccaia breach flows across the inundated areas and overtops the levee from the outside, re-entering the river along this bend.

The temporal sequence highlights a markedly different behaviour compared to the Steccaia breach. Overtopping initiates around 20:30 on 16 May 2023, and erosion develops over a much longer time scale, reaching a quasi-equilibrium configuration only after approximately 22 hours. This slower evolution may be explained by the hydraulic conditions associated with return flow. As water re-enters the main channel from the inundated areas, the river is already characterized by high water levels, so that the returning flow is consistently backwatered by the river stage. Under these conditions, the flow remains subcritical and does not develop a freely accelerating flow along the inner levee slope. As a consequence, shear stresses acting on the embankment surface are significantly reduced, leading to a lower erosive capacity and slower breach development.

This behaviour is illustrated in Fig. 14a–b, which shows a representative cross-section of the levee and water levels at two distinct times during the event (see Fig. 13 for the section location). Shortly after the onset of overtopping, the levee is still largely intact, and the water level difference between the inundated areas outside the levee system and the river is small, resulting in a subcritical, submerged flow. At a later time, although river water levels have decreased, the levee has already undergone significant erosion, so that the head difference remains small, and the returning flow remains subcritical. As a consequence, flow velocities are limited, leading to reduced erosive capacity.

https://doi.org/10.5194/egusphere-2026-2992
Preprint. Discussion started: 24 June 2026

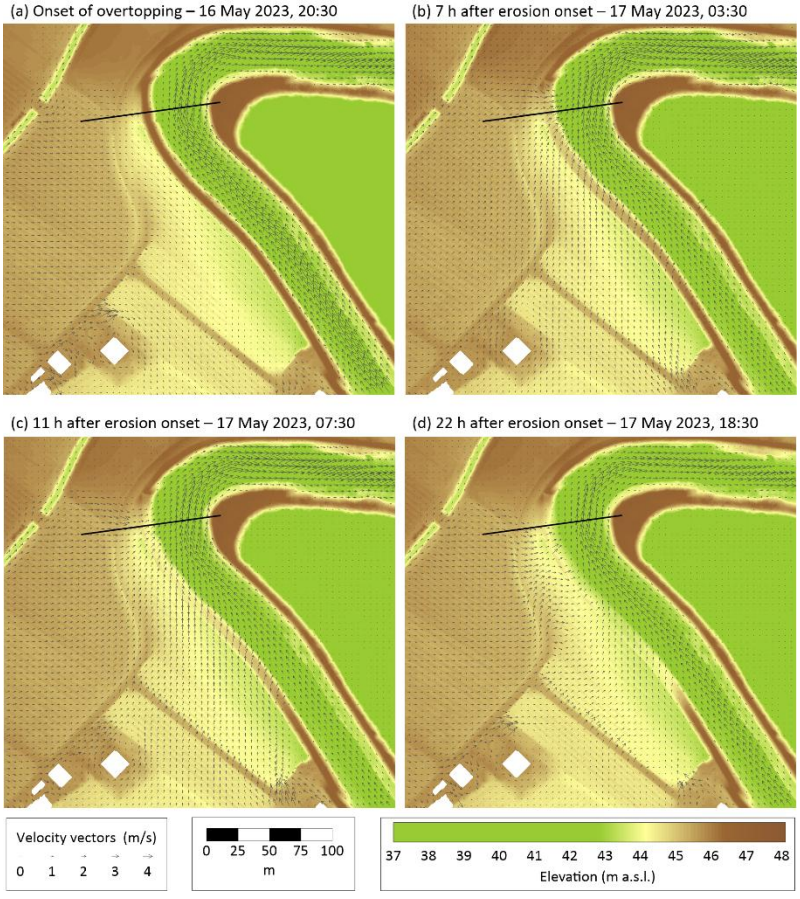

Figure 13: Temporal evolution of the Biancanigo levee breach (B5) during the 16–19 May 2023 flood event. The figure illustrates the progressive erosion of the levee and the associated velocity field, highlighting the development of return flow toward the river channel. Velocity vectors are represented every five cells in both horizontal directions for clarity. The location of the cross-section shown in Fig. 14 is also indicated.

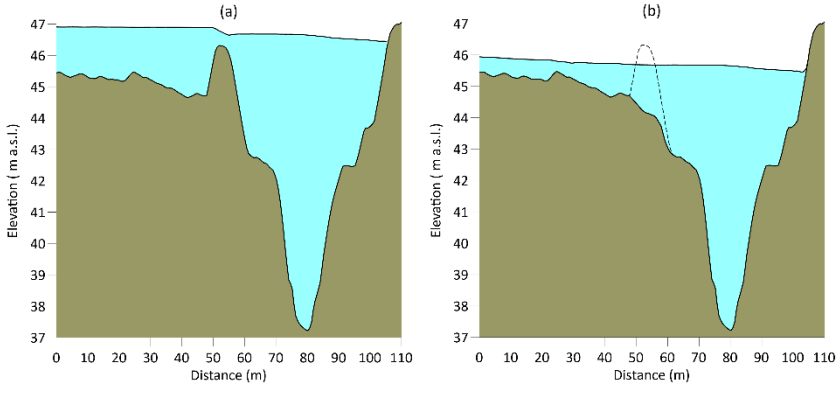

Figure 14: Representative cross-section of the river at the Biancanigo breach (B5) location, showing bed elevation and water levels at two distinct stages of the 16–19 May 2023 flood event: (a) 21:30 on 16 May 2023, shortly after the onset of overtopping, and (b) 08:30 on 17 May 2023, after significant erosion has occurred. In panel (b), the dashed line indicates the initial levee profile prior to erosion. The section location is shown in Fig. 13.

https://doi.org/10.5194/egusphere-2026-2992
Preprint. Discussion started: 24 June 2026

The comparison between pre-event, post-event, and simulated final topography (Fig. 15) reveals a more complex erosion pattern than that observed for localized breaches. In the post-event DTM, the levee is eroded along extended portions, while some segments almost remain intact. In contrast, the simulation predicts a more continuous erosion of the levee, resulting in a smoother final morphology. It is also apparent that a vertical offset of approximately 0.2 m exists between the pre- and post-event DTMs. This aspect is further analysed and discussed in Section 5.

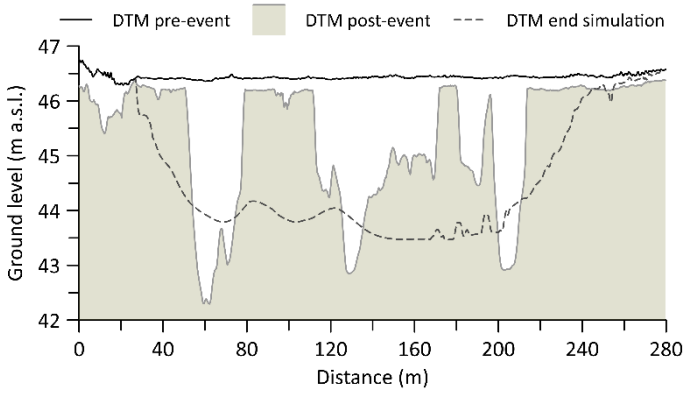

Figure 15: Comparison between pre-event, post-event, and simulated topography at the Biancanigo levee breach (B5). The pre- and post-event topographies are derived from the LiDAR-based DTM, while the simulated configuration corresponds to the final state of the morphodynamic model.

4.3 Flood inundation patterns and model performance

The spatial distribution of the maximum water depths reached during the event is shown in Fig. 16. The map represents the envelope over the entire simulation period, rather than a snapshot at a specific time. The simulated inundation pattern highlights the main flow pathways and the spatial extent of flooding across the study area, with deeper water levels concentrated near the levee breaches and along preferential flow directions. The figure also highlights the significant influence of road and railway embankments on the spatial distribution of maximum water depths, with water accumulating upstream of these structures due to the limited number of openings allowing flow passage.

It should be noted that the inundation domain extends further north than the area shown in Fig. 16. However, this portion of the domain was also affected by flooding from the Santerno River, which flows to the west of the Senio River. During the event, breaches occurred along the right levee of the Santerno, and the resulting floodwaters merged with those spilling from the left bank of the Senio. For this reason, a direct comparison between simulated and observed inundations in these areas would not be meaningful. A more rigorous assessment would require a coupled modelling of the two river systems, which was beyond the scope of the present study.

https://doi.org/10.5194/egusphere-2026-2992
Preprint. Discussion started: 24 June 2026

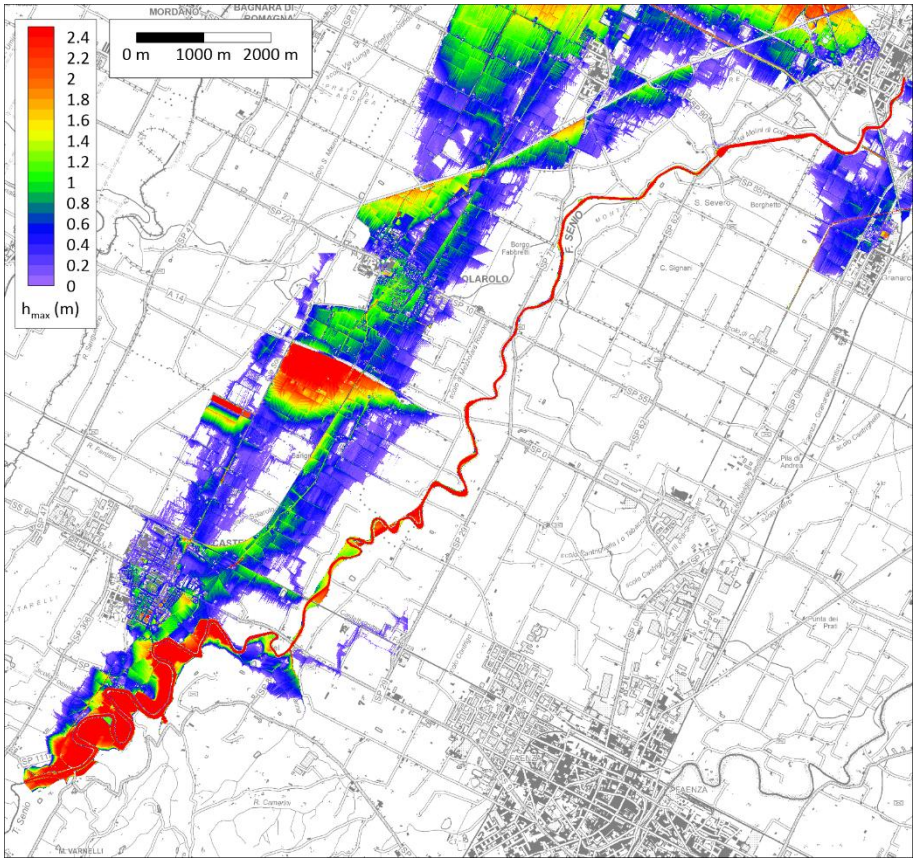

Figure 16: Maximum simulated water depths during the 16–19 May 2023 flood event. Colors represent the maximum water depth reached at each location over the entire simulation period (Base map: © Regione Emilia-Romagna Geoportal).

A detailed spatial comparison between simulated and observed inundated areas, including the full contingency classification (true positives TP, false positives FP, false negatives FN, and true negatives TN), is provided in Appendix A (Fig. A5). To quantitatively assess model performance, the spatial agreement metrics described in Section 3 were computed, and the results are summarized in Table 5 for both the entire domain and the urban area of Castel Bolognese. A complete comparison including all tested morphodynamic parameter sets is provided in Appendix A (Table A1), showing that similar flood extents are obtained for parameter sets 1 and 2 despite differences in breach morphodynamic behaviour.

Over the entire domain, the comparison indicates a generally good agreement between simulated and observed flood extent, with a Jaccard index of 0.67. These results reflect both the complexity of the event and the spatial variability of flood processes across the domain. The true positive rate (TPR) of 0.85 indicates that the model correctly identifies most of the flooded areas, while the corresponding false positive rate (FPR) of 0.10 suggests a moderate overestimation of inundated areas.

A more detailed analysis was carried out over the urban area of Castel Bolognese, which represents the most densely urbanized portion of the study domain and the most damaged area during the event. The spatial distribution of maximum water depths in this area is shown in Fig. 17. The map highlights zones characterized by high water depths (red colors), exceeding 1.4 m.

https://doi.org/10.5194/egusphere-2026-2992
Preprint. Discussion started: 24 June 2026

These areas correspond to locally depressed portions of the terrain, such as open semi-underground spaces or underpasses below the railway embankment crossing the town from north-west to south-east. Additional zones of high water depth are located close to the river and likely correspond to former floodplain areas excluded from the levee system. Intermediate water depths (green to orange colors, approximately between 0.4 and 1.4 m) occur in areas where flow is locally obstructed by infrastructural embankments, which induce backwater effects and water accumulation upstream. In the remaining portions of the urban area, water depths generally range between 0.2 m and 0.4 m. Considering the typical urban structure of Castel Bolognese, where many buildings include basements or semi-underground levels, these water depths are sufficient to explain the extensive damages observed during the event.

For the evaluation of performance metrics, the domain was restricted to the urban area shown in the same Fig. 17. This choice allows a more meaningful interpretation of the metrics, avoiding artificial inflation of true negative values associated with large non-flooded areas outside the zone of interest.

In this area, the agreement between simulated and observed flood extent is very good, with a Jaccard index of 0.85. The TPR increases to 0.92, while the FPR is slightly higher (0.15), indicating a modest overestimation of inundated areas. Only a limited area located in the north-western sector appears to be flooded in the simulation, while it is not included in the Civil Protection map. These discrepancies will be further discussed in Section 5.

Further validation was carried out using point-based observations of maximum water depth, collected within the urban area at a limited number of locations (nine points indicated in Fig. 17) and derived from post-event surveys and eyewitness reports. A quantitative comparison was performed by computing standard error metrics between observed and simulated water depths. The obtained values (RMSE ≈ 0.14 m, MAE ≈ 0.11 m, and bias ≈ -0.02 m) indicate a good agreement, considering both the limited number of observations and the uncertainty associated with the field estimates. The full dataset of observation points, including their spatial coordinates and corresponding water depth values, is provided in Appendix A (Table A2).

Table 5 – Quantitative comparison between simulated and observed flood extent based on the Jaccard index (J) and contingency metrics (TP, FP, FN, TN), including derived performance indicators (TPR, FPR).

	J	TP (km^2)	FP (km^2)	FN (km^2)	TN (km^2)	TPR (-)	FPR (-)
Entire domain	0.67	22.08	7.17	3.75	66.15	0.85	0.10
Castel Bolognese urban area	0.85	1.39	0.11	0.13	0.64	0.92	0.15

Regarding maximum flow velocities, values remain relatively low (generally below ~1 m/s) over most rural areas. Higher velocities (up to 4 m/s) are observed in the vicinity of levee breaches and at locations where water either overtops or flows under elevated embankments. The complete spatial distribution of maximum velocities is reported in Appendix A (Fig. A6). Figure 18 shows a detailed view of the urban area of Castel Bolognese, where relatively high velocities (up to about 4 m/s) are also observed along some streets, particularly those aligned with the main flow direction (southwest–northeast). It is worth noting that the high spatial resolution of the simulation, combined with the building-hole approach, allows the identification

https://doi.org/10.5194/egusphere-2026-2992
Preprint. Discussion started: 24 June 2026

of these preferential flow paths within the urban fabric. Such features would likely not be captured using coarser spatial resolutions or simplified representations of urban areas, such as approaches based solely on increased roughness.

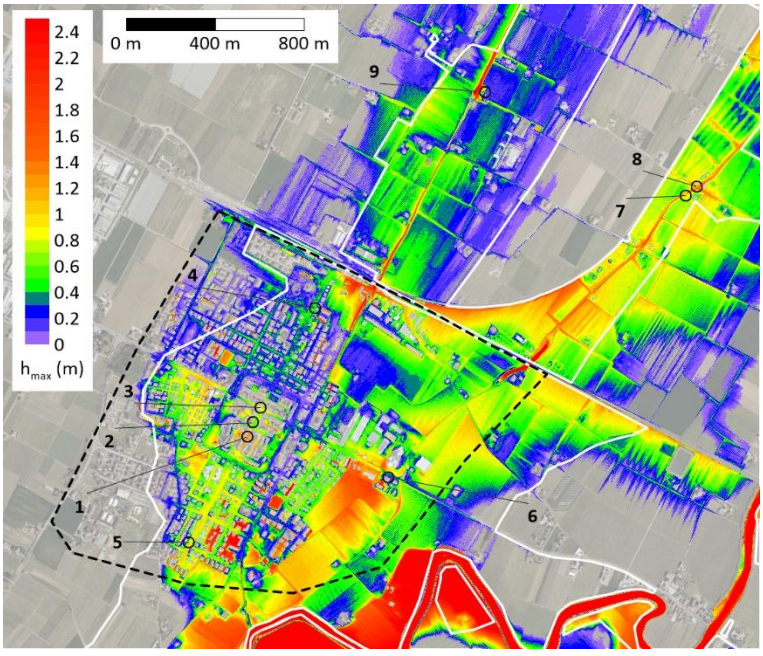

Figure 17: Maximum simulated water depths in the urban area of Castel Bolognese during the 16–19 May 2023 flood event. Colors represent the maximum water depth at each location. The observed flood extent mapped by Civil Protection authorities is shown by the white outline. The evaluation domain used for the computation of performance metrics (Jaccard index and contingency indicators) is delineated by the black dashed boundary. Markers indicate the locations where observed and simulated maximum water depths were compared (Base map: © Regione Emilia-Romagna Geoportal).

https://doi.org/10.5194/egusphere-2026-2992
Preprint. Discussion started: 24 June 2026

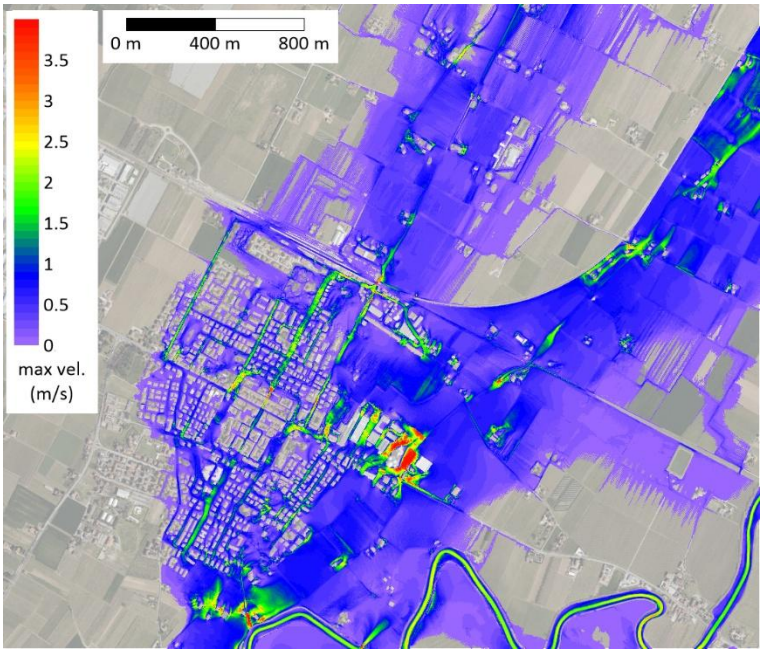

Figure 18: Maximum simulated flow velocities in the urban area of Castel Bolognese during the 16–19 May 2023 flood event. The map highlights preferential flow paths along streets and in the vicinity of infrastructural elements, where locally high velocities occur (Base map: © Regione Emilia-Romagna Geoportal).

Finally, the temporal evolution of flood propagation was analysed through the computation of flood arrival times over the entire simulated domain, as shown in Fig. 19. The map represents the time at which the flood front reaches each location, thus providing a spatial overview of the propagation dynamics across the lowland areas. Some locations, where eyewitness information was available, are indicated in the figure. Arrival times were collected in these areas in local daylight saving time (UTC+2) and converted into UTC+1. Testimonies indicate that the flood front reached Biancanigo at approximately 21:00 and Boccaccio at approximately 22:00, while it reached the town center of Castel Bolognese at approximately 23:00 (May 16). Additional observations collected in a small residential area located north of the railway line in Castel Bolognese indicate that the flood front arrived at approximately 00:30 (May 17), corresponding to about 24.5 hours from the beginning of the simulation. For Solarolo, available sources suggest that the arrival of floodwaters occurred during the early hours of May 17, with inundation already evident at dawn (≈ 04:45–05:00) and reports of initial water arrival in the indicated area at around 07:00 (31 h). These observations are in very good agreement with the simulated arrival times, confirming that the coupled hydrodynamic–morphodynamic model is able to reproduce not only the spatial extent of inundation but also its temporal evolution. This represents a particularly challenging aspect of flood modelling in embanked systems, where the timing of levee breaches strongly controls flood propagation dynamics.

https://doi.org/10.5194/egusphere-2026-2992
Preprint. Discussion started: 24 June 2026

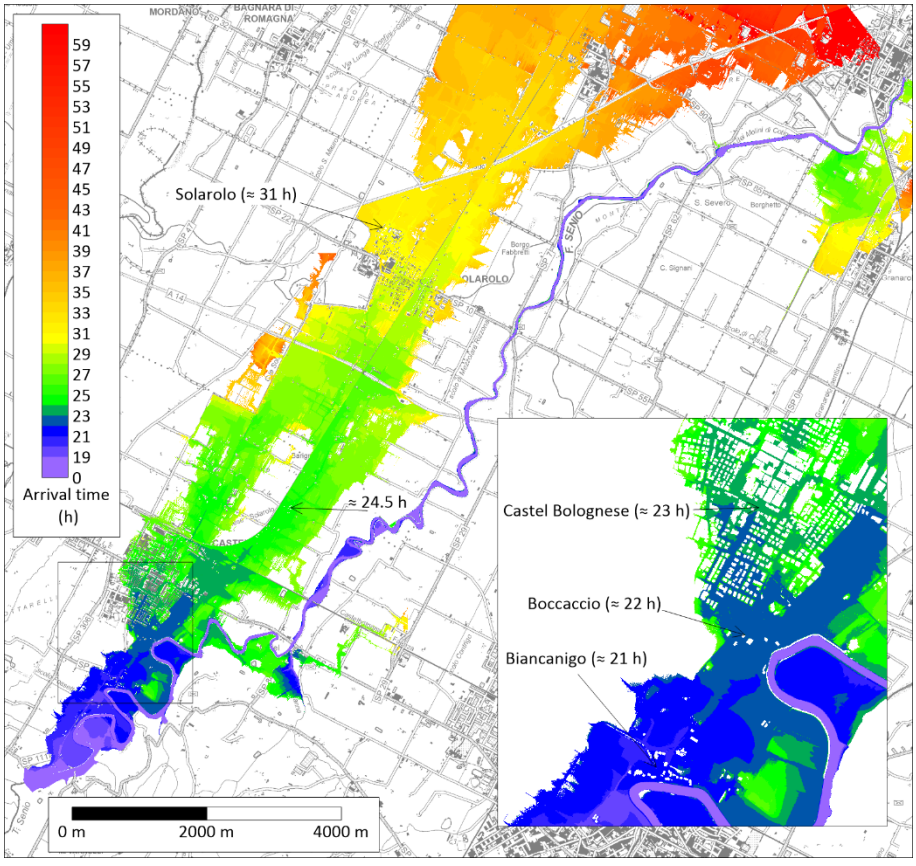

Figure 19: Simulated flood arrival times over the inundated area during the 16–19 May 2023 flood event. Colors represent the time of arrival of the flood front, expressed in hours from 00:00 on 16 May 2023 (UTC+1). Arrows indicate locations where eyewitness observations are available. The inset shows a detailed view of the area close to the levee breaches (Base map: © Regione Emilia-Romagna Geoportal).

5 Discussion

5.1 Role of levee breaches in flood propagation

The results highlight the dominant role of levee breach processes in controlling both flood wave propagation and inundation dynamics in embanked lowland systems. The coupled hydrodynamic–morphodynamic modelling approach adopted in this study allows these processes to be represented explicitly, capturing the strong interaction between channel flow, levee erosion, and floodplain exchange.

In particular, the analysis of the reconstructed hydrographs shows that the evolution of water levels and discharges along the river is strongly influenced by the opening of breaches. The rapid drop in water levels observed after the peak stage at Castel Bolognese gauging station is directly linked to flow diversion through levee breaches, while the subsequent deviation from the

https://doi.org/10.5194/egusphere-2026-2992
Preprint. Discussion started: 24 June 2026

typical exponential recession behaviour, visible as a change in the curvature of the hydrograph, is associated with delayed return flows from inundated areas.

The case of the Biancanigo breach further demonstrates that the longitudinal evolution of discharge along the river is not necessarily monotonic. In contrast to classical flood wave propagation without lateral exchanges, discharge may locally increase downstream due to re-entry of water previously spilled onto the inundated areas outside the levee system. These results emphasize the need for physically based modelling approaches capable of representing both outflow and return-flow mechanisms.

These findings are consistent with previous studies highlighting the dominant role of breach processes in flood dynamics and residual risk assessment (Wahl, 1998; Morris et al., 2007; Apel et al., 2009; Vorogushyn et al., 2009).

5.2 Uncertainty and model limitations

Despite the overall good agreement between simulated and observed results, some discrepancies remain, particularly in the representation of breach geometry and local inundation patterns.

The first source of uncertainty is related to the representation of topography. Even small errors in elevation (on the order of decimetres, which are typical of LiDAR-derived DTMs) can influence the exact location where overtopping initiates. As shown in Fig. 12 and Fig. 15, a vertical offset of approximately 0.1–0.2 m is observed between the pre-event and post-event DTMs. Elevation uncertainties of this magnitude may significantly affect the onset of overtopping and the subsequent development of breaches, especially in low-gradient embanked systems. In addition, the filtering of vegetation during LiDAR post-processing may introduce local inaccuracies, particularly in areas characterized by dense or irregular vegetation cover.

Second, the adopted values of the erodibility parameters are subject to significant uncertainty. In the absence of site-specific geotechnical measurements, a single set of parameters was applied along the entire levee system. However, the actual levee material may be heterogeneous both along the embankment and across its vertical profile. In particular, in the Biancanigo reach, the levee may be more erodible than assumed, especially considering that erosion develops from the landward side toward the channel.

It is worth noting that increasing the erodibility coefficient k_d, which directly controls the erosion rate, does not necessarily lead to a longer eroded reach. On the contrary, as highlighted by Dazzi et al. (2019) and Dazzi and Mignosa (2026), higher values of k_d may induce a more rapid incision in the most vulnerable portions of the levee, leading to a faster drop in water levels on the levee crest. This, in turn, can reduce overtopping elsewhere and preserve portions of the levee, resulting in multiple breaches separated by segments that remain partially or entirely intact, as sometimes observed in the field.

Third, the morphodynamic model relies on simplified assumptions. In particular, erosion is described using a linear excess shear stress formulation, whereas real erosion processes in cohesive embankments are governed by more complex mechanisms, including soil structure, compaction, and progressive failure.

Finally, the representation of urban areas may also contribute to discrepancies in flood extent. The use of the “building hole” approach neglects water storage within buildings, such as basements and semi-underground spaces. In addition, the urban

https://doi.org/10.5194/egusphere-2026-2992
Preprint. Discussion started: 24 June 2026

drainage network was not explicitly represented in the model. These simplifications may lead to a slight overestimation of water depth and flood extent in urban areas, as observed in the north-western sector of Castel Bolognese.

5.3 Sensitivity to morphodynamic parameters and hydraulic forcing

The sensitivity analyses carried out within this study indicate that the critical shear stress (τ_c) has a relatively limited influence on the simulation results. This behaviour can be explained by the fact that, during overtopping conditions, the effective shear stresses exerted by the flow largely exceed the critical threshold for erosion.

As an illustrative example, Fig. 20a shows the spatial distribution of the bed shear stress computed by the model around the La Steccaia breach (B1) at a representative time of the simulation, when several breaches have already developed. In this area, shear stress values approach or exceed 100 Pa, which is one or more orders of magnitude higher than typical critical shear stress values for cohesive materials (see Fig. 6). Under such conditions, erosion is controlled primarily by the erodibility coefficient k_d, which governs the rate of material removal, while the influence of τ_c becomes secondary. This explains why variations in τ_c ithin plausible ranges have a limited impact on the overall breach evolution, whereas changes in k_d significantly affect both the rate of erosion and the resulting breach geometry.

However, this is not always the case. Fig. 20b shows the spatial distribution of bed shear stress at a later time of the simulation for the distributed return-flow breach at Biancanigo (B5). In this situation, due to the backwater effect exerted by the river stage, the returning flow remains hydraulically subcritical and does not develop into a freely accelerating flow along the inner levee slope (see Fig. 14a). As a result, shear stresses remain significantly lower (on the order of 10 Pa) than those observed under non-backwatered breach conditions. In such cases, the adopted value of the critical shear stress may become a controlling factor, potentially determining whether erosion occurs or not.

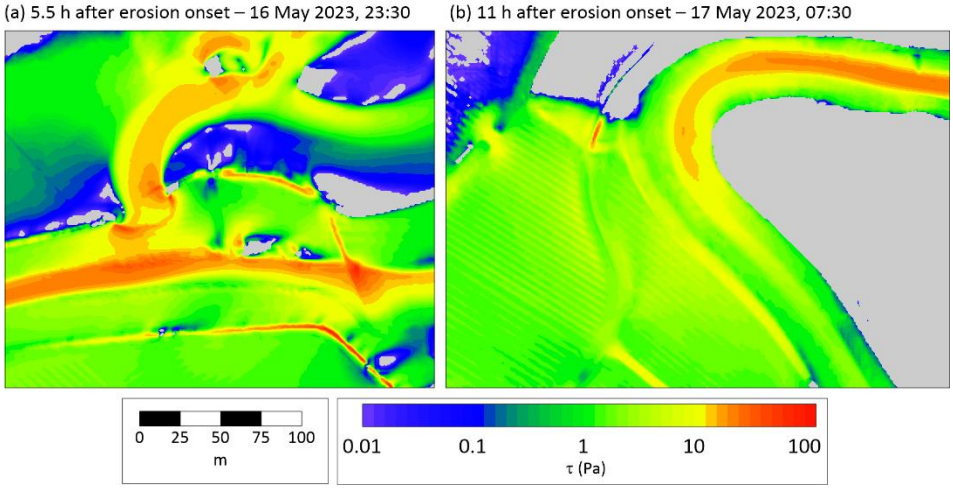

Figure 20: Spatial distribution of bed shear stress during the 16–19 May 2023 flood event at two representative times of the simulation: (a) La Steccaia breach (B1) and (b) Biancanigo breach (B5). The circled areas highlight the location of the breaches. In panel (a), shear stress values reach 100 Pa, significantly higher than typical critical thresholds for cohesive materials. In contrast, panel (b) shows much lower shear stresses (on the order of 10 Pa), associated with backwater conditions and return-flow dynamics.

https://doi.org/10.5194/egusphere-2026-2992
Preprint. Discussion started: 24 June 2026

A broader comparison of all tested parameter sets (Table A1 in Appendix A) provides further insight into model sensitivity. The comparison reported in Table A1 indicates that the simulated flood extent is relatively insensitive to variations in morphodynamic parameters within plausible ranges, as similar agreement metrics are obtained for parameter sets 1 and 2. However, these parameter sets produce significantly different breach dynamics and flow evolution along the river. This result suggests that flood extent alone may not be sufficient to constrain morphodynamic parameters, highlighting the importance of using additional indicators, such as water levels and temporal dynamics, in model calibration.

5.4 Implications of multiple simultaneous levee breaches

The 16–19 May 2023 event highlighted an unusual and particularly relevant aspect of flood dynamics in embanked systems. In the authors' experience, it is relatively uncommon for multiple levee breaches to occur simultaneously within a limited river reach. Typically, the formation of a breach in the upstream portion of the system leads to a reduction in discharge and water levels downstream, thereby limiting the likelihood of additional failures.

This assumption underlies previous work carried out within the RESILIENCE project (Ferrari et al., 2020), in which flood hazard maps for the Emilia-Romagna region–also developed in the framework of the EU Floods Directive (2007/60/EC) – were obtained by simulating individual breach scenarios within hydraulically bounded compartments. In that framework, multiple potential breach locations were considered, but failures were assumed to occur independently rather than simultaneously, and final hazard maps were derived from the envelope of individual simulations. In contrast, the May 2023 flood event along the Senio River was characterized by the simultaneous occurrence of ten levee breaches, distributed along both riverbanks within a relatively short reach. Additional breaches occurred during the same event along the neighbouring Santerno and Lamone rivers, located immediately to the west and east of the Senio, respectively.

These observations suggest that the combined effect of multiple simultaneous breaches may lead to flood scenarios that differ significantly from those obtained by superimposing independent single-breach simulations. Assessing whether such compound scenarios result in more severe hazard conditions remains an open question and is beyond the scope of the present study, although it represents a relevant direction for future research.

5.5 Implications for stage–discharge relationships in the presence of levee breaches

The presence of levee breaches also has important implications for the interpretation of stage–discharge relationships. Figure 21 shows the relationship between water level and discharge at three representative sections for the May 2023 events: Tebano, Castel Bolognese, and a section between the two gauging stations located upstream of the Biancanigo breach (S6). It should be noted that, due to the two-dimensional nature of the model, water level is not uniform across a cross section, and the concept of a single stage–discharge relationship becomes less well defined. For the Tebano and Castel Bolognese stations, water levels were extracted at grid points located close to the gauging stations, whereas for the section upstream of Biancanigo a point located near the center of the channel was selected.

https://doi.org/10.5194/egusphere-2026-2992
Preprint. Discussion started: 24 June 2026

In all sections, the stage–discharge relationship is not unique, but it exhibits a hysteresis loop. This is a well-known effect, particularly in rivers characterized by low bed slopes, where under unsteady flow conditions the friction slope depends not only on water level but also on pressure gradients and inertial effects, which vary in time, leading to hysteretic stage–discharge relationships (e.g., Di Baldassarre and Montanari, 2009; Petersen-Øverleir, 2004). However, this non-uniqueness is greatly amplified in the presence of levee breaches, as clearly observed at the section upstream of Biancanigo during the second event, as a consequence of the multiple breaches occurring both upstream and downstream. At this location, for example, the same discharge value (approximately 110 m³/s) corresponds to markedly different water levels depending on whether the flow is in the rising limb, immediately after breach formation, or during the recession phase (Fig. 21b).

At the Tebano section (Fig. 21a), the comparison between the two events shows that, for the same water level (higher than 48.5 m a.s.l.), higher discharges are obtained during the second event. This effect is due to the lowering of water levels induced by levee breaches, which modify the hydraulic conditions along the river. In the first event, where no significant breaches occurred, this effect is absent, and water levels corresponding to a given discharge are generally higher.

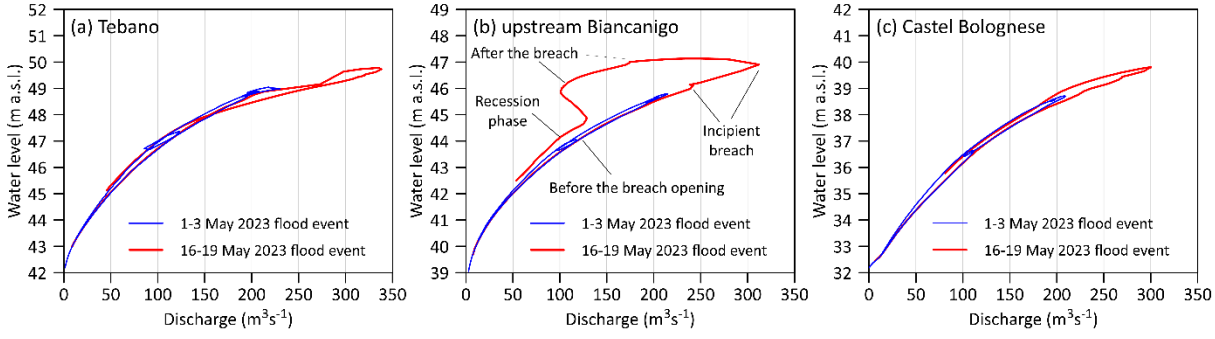

Figure 21: Stage–discharge relationships at selected cross sections along the Senio River during the May 2023 flood events: (a) Tebano gauging station; (b) Section S6 located upstream of the Biancanigo breach; (c) Castel Bolognese gauging station. The diagrams highlight the non-uniqueness of the stage–discharge relationship and the amplification of hysteresis effects in the vicinity of levee breaches.

These results indicate that, in the presence of levee breaches, stage–discharge relationships evolve dynamically and cannot be represented by a single-valued rating curve. This has important implications for hydraulic modelling and flood reconstruction. In particular, the common practice of deriving discharge hydrographs from observed water levels using fixed stage–discharge rating curves may introduce significant errors in the presence of breaches. As a consequence, when such hydrograph is used as upstream boundary condition, these errors may propagate through the model and affect the calibration process.

These findings highlight the need for caution when using traditional rating curves under highly dynamic conditions and support the adoption of fully coupled hydrodynamic–morphodynamic approaches for the reconstruction of flood events in embanked river systems.

https://doi.org/10.5194/egusphere-2026-2992
Preprint. Discussion started: 24 June 2026

6 Conclusions

This paper presents a high-resolution hydrodynamic–morphodynamic reconstruction of the 16–19 May 2023 flood event along the Senio River, with explicit simulation of multiple levee breach formation and evolution. The adopted modelling approach enables the coupled representation of flow dynamics, breach development, and inundation of the surrounding areas within a physically consistent framework. The model results were successfully validated against a comprehensive dataset, including hydrometric records, high-resolution pre- and post-event topography, flood extent mapping, and eyewitness observations, which overall confirm that this approach is suitable for modelling challenging case studies with multiple simultaneous levee breaches and can support advanced analyses of flood dynamics and residual risk in embanked river systems.

The results also highlight the dominant role of levee breaches in controlling flood propagation in embanked low-gradient systems. On the one hand, breach evolution strongly influences both water levels and discharges along the river: rating curves become strongly non-unique and evolve dynamically over time, limiting their applicability for deriving reliable discharge hydrographs. On the other hand, complex interactions between the channel and the surrounding inundated areas may be generated, including both flow diversion and return-flow mechanisms.

Future work should focus on improving the characterisation of levee material properties, accounting for the spatial variability of erodibility parameters, and further investigating the interaction between channel processes and urban flood dynamics. In addition, the role of multiple simultaneous levee breaches in shaping flood hazard deserves further investigation, particularly in relation to current hazard assessment approaches based on independent breach scenarios.

https://doi.org/10.5194/egusphere-2026-2992
Preprint. Discussion started: 24 June 2026

Appendix A

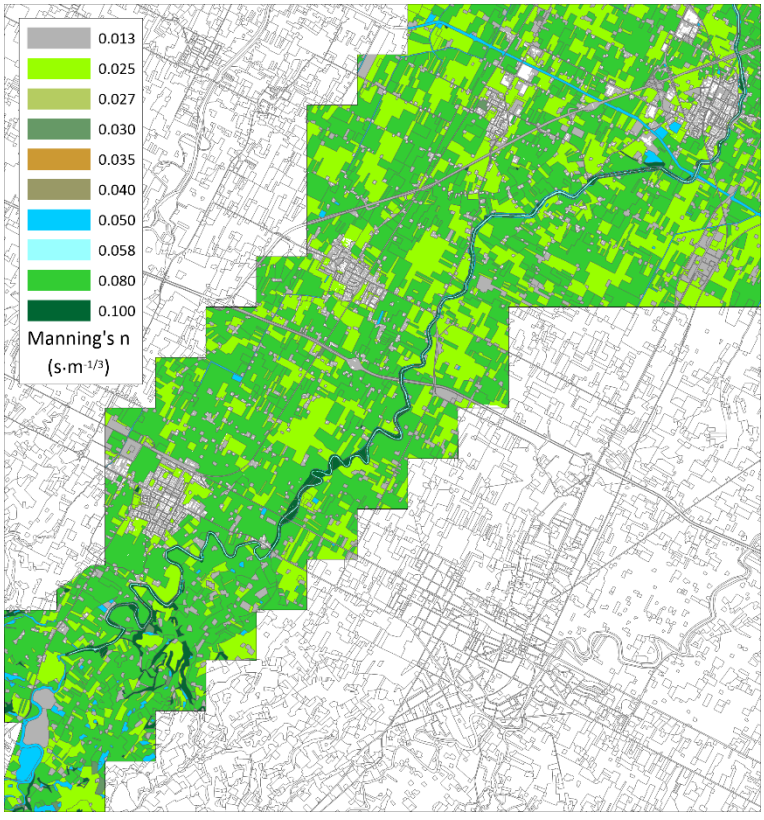

Figure A1: Spatial distribution of Manning's roughness coefficients over the computational domain. Roughness values in the river channel result from calibration, while values outside the levees are assigned based on CORINE land-use data.

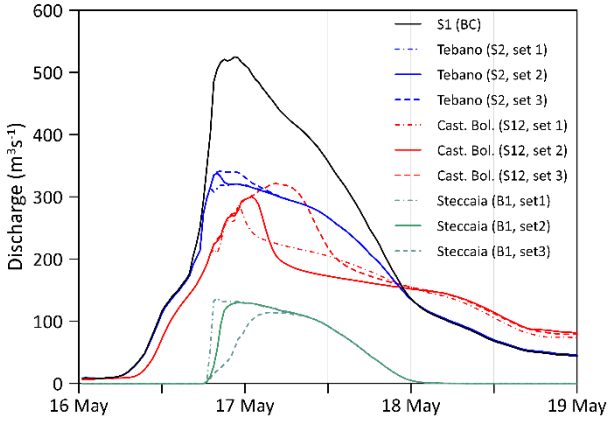

Figure A2: Reconstructed inflow hydrograph at the upstream boundary and simulated discharges along the Senio River reach for the three tested morphodynamic parameter sets (sets 1–3) during the 16–19 May 2023 flood event. The figure includes the simulated discharges at Tebano and Castel Bolognese, as well as the discharge flowing through the "La Steccaia" breach. Differences among parameter sets are particularly evident at Castel Bolognese, highlighting the influence of upstream breach dynamics on flow distribution along the river.

https://doi.org/10.5194/egusphere-2026-2992
Preprint. Discussion started: 24 June 2026

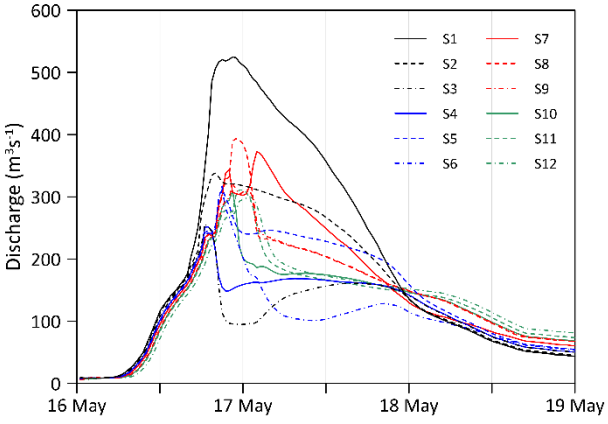

Figure A3: Simulated discharge at selected cross sections along the Senio River during the 16–19 May 2023 flood event (morphodynamic parameter set 2). The figure illustrates the combined effects of flow diversion through levee breaches and subsequent return flows along the modeled reach.

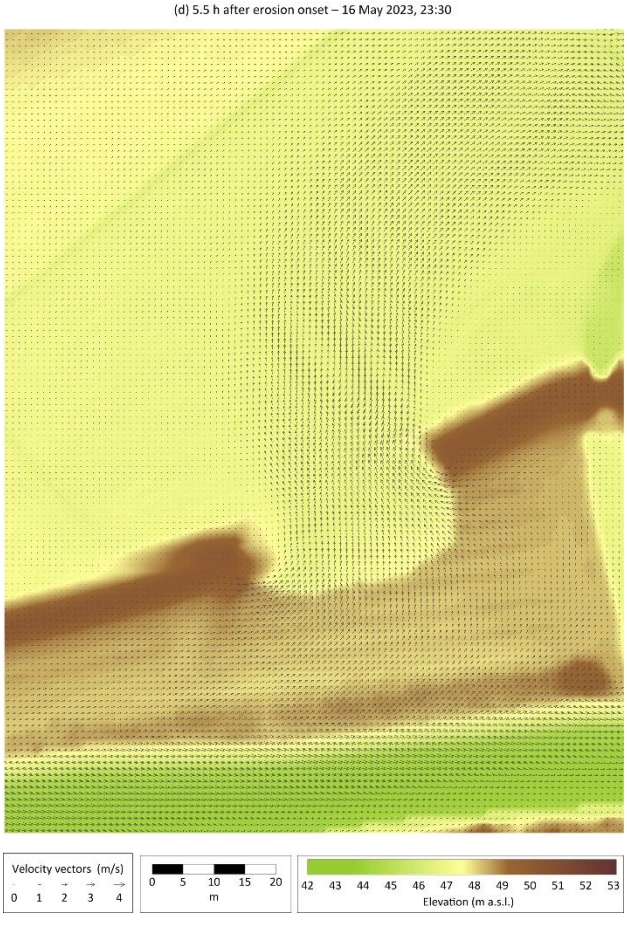

Figure A4: Detailed view of the velocity field at the La Steccaia breach at 23:30 on 16 May 2023 (corresponding to panel (d) in Fig. 11). All computational velocity vectors are shown, highlighting the fine spatial resolution of the simulation based on a 1 × 1 m computational grid.

https://doi.org/10.5194/egusphere-2026-2992
Preprint. Discussion started: 24 June 2026

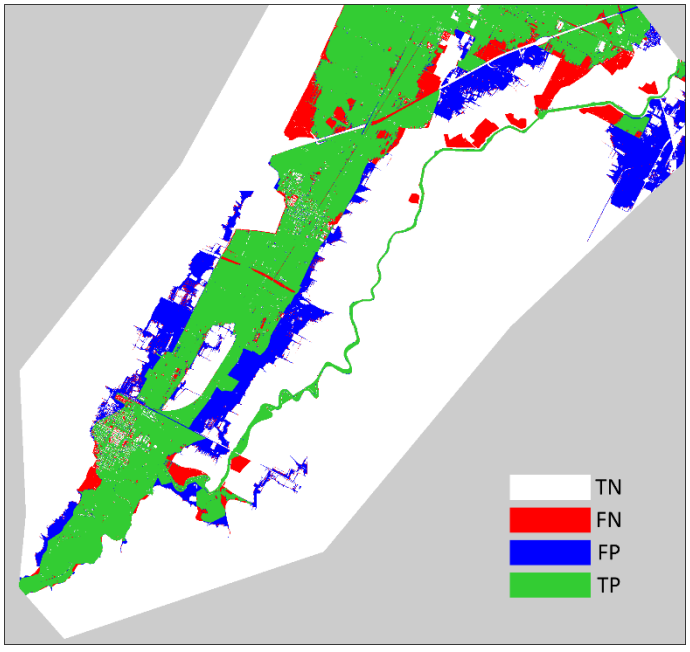

Figure A5: Spatial comparison between simulated and observed flood extent based on the contingency classification. Colors indicate true positives (TP), false positives (FP), false negatives (FN), and true negatives (TN), as defined in Section 3. The grey area represents portions of the computational domain excluded from the evaluation of the performance metrics.

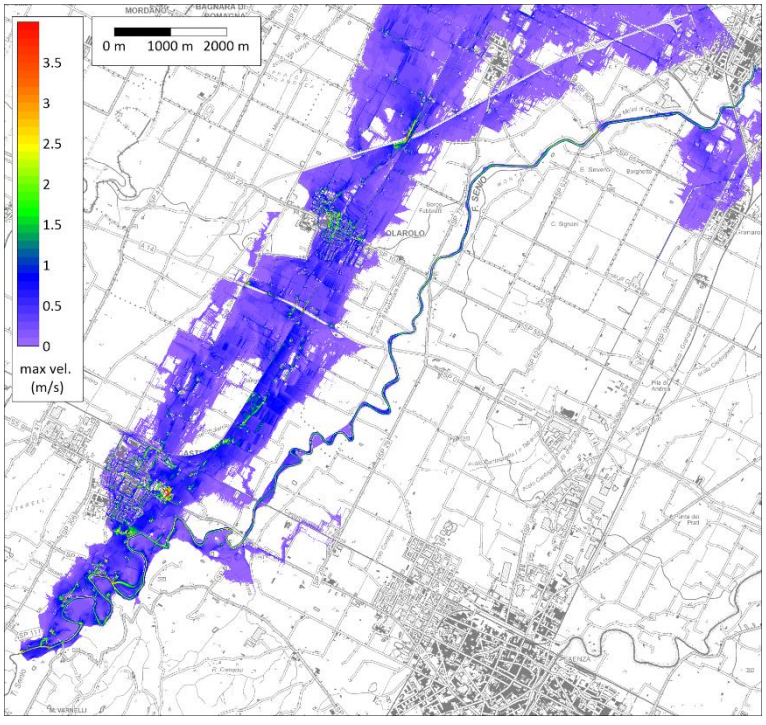

Figure A6: Maximum simulated flow velocities during the 16–19 May 2023 flood event. Colors represent the maximum velocity reached at each location over the entire simulation period (Base map: © Regione Emilia-Romagna Geoportal).

https://doi.org/10.5194/egusphere-2026-2992
Preprint. Discussion started: 24 June 2026

Table A1 – Performance metrics for all tested morphodynamic parameter sets.

Set N.	τ_c (Pa)	k_d (cm³/(N·s))	Domain	J (-)	TP (km²)	FP (km²)	FN (km²)	TN (km²)	TPR (-)	FPR (-)
1	0.1	1.0	Entire domain	0.67	20.75	5.16	5.08	68.16	0.80	0.07
			Castel Bolognese urban area	0.85	1.40	0.12	0.12	0.63	0.92	0.16
2	1.0	0.3	Entire domain	0.67	22.08	7.17	3.75	66.15	0.85	0.10
			Castel Bolognese urban area	0.85	1.39	0.11	0.13	0.64	0.92	0.15
3	10.0	0.1	Entire domain	0.57	18.49	6.39	7.34	66.93	0.72	0.09
			Castel Bolognese urban area	0.83	1.33	0.08	0.19	0.68	0.87	0.10

Table A2 – Point-based comparison between observed and simulated maximum water depths in the urban area of Castel Bolognese. The table reports the geographic coordinates of the observation points and the corresponding observed and simulated values, derived from post-event surveys and eyewitness reports, used for the computation of error metrics (RMSE, MAE, and bias).

Id	Lat. N (°)	Long. E (°)	Max water depth (m) Simulated	Max water depth (m) Observed	Error (m) Sim.-Obs.
1	44.318457	11.798904	1.33	1.00	0.33
2	44.319023	11.799225	0.74	0.75	-0.01
3	44.319607	11.799702	0.93	1.10	-0.17
4	44.323553	11.802958	0.46	0.50	-0.04
5	44.314257	11.795398	0.90	1.00	-0.1
6	44.316626	11.806738	0.06	0.10	-0.04
7	44.327597	11.824036	0.93	0.80	0.13
8	44.327964	11.824669	1.29	1.35	-0.06
9	44.332073	11.812941	0.31	0.20	0.11

Code and data availability

The original digital terrain model (DTM) is available from the Emilia-Romagna Region Geoportal (https://geoportale.regione.emilia-romagna.it/catalogo/dati-cartografici/altimetria/layer-60), subject to the applicable data access regulations. However, the terrain model used in this study was further processed and locally modified as described in the manuscript.

Water level observations used for model setup and validation are available from ARPAE Emilia-Romagna (https://simc.arpae.it/dext3r/), subject to the applicable data access regulations. The upstream discharge hydrograph adopted in the simulations was not directly measured, but reconstructed through the procedure described in the manuscript.

Selected model outputs supporting the results of this study are available from the corresponding author upon reasonable request.

The PARFLOOD model is available for non-commercial scientific collaboration upon request.

https://doi.org/10.5194/egusphere-2026-2992
Preprint. Discussion started: 24 June 2026

Author contributions

Francesca Aureli and Paolo Mignosa conceived the study. Francesca Aureli and Sara Carta performed the numerical simulations. Susanna Dazzi developed and implemented the morphodynamic modelling module. All authors contributed to data analysis, interpretation of results, and manuscript preparation.

Competing interests

A The authors declare that they have no conflict of interest.

Acknowledgements

The authors acknowledge the Agenzia regionale per la sicurezza territoriale e la protezione civile della Regione Emilia-Romagna (Emilia-Romagna Agency for Territorial Safety and Civil Protection) for providing hydrological and topographic data. Orthophotos and technical cartography were obtained from the Emilia-Romagna Region Geoportal. The authors also acknowledge Luca Mora for his contribution to the numerical simulations. The authors gratefully acknowledge Mr. Domenico Sportelli, Councillor Ignazio Belfiore, and other residents of Castel Bolognese for providing valuable information on the flood event investigated in this study and for their support in gathering field observations. This research benefited from the High-Performance Computing (HPC) facility of the University of Parma.

References

Apel, H., Aronica, G. T., Kreibich, H., and Thieken, A. H.: Flood risk analyses—how detailed do we need to be?, Nat. Hazards, 49, 79–98, 2009, https://doi.org/10.1007/s11069-008-9277-8.

Arcement, G. J. and Schneider, V. R.: Guide for Selecting Manning's Roughness Coefficients for Natural Channels and Flood Plains, U.S. Geological Survey Water-Supply Paper 2339, 1989, https://doi.org/10.3133/wsp2339.

Aricò, C., Nasello, C., and Tucciarelli, T.: Using unsteady-state water level data to estimate channel roughness and discharge hydrograph, Adv. Water Resour., 32, 1223–1240, 2009, https://doi.org/10.1016/j.advwatres.2009.05.001.

Aronica, G. T., Bates, P. D., and Horritt, M. S.: Assessing the uncertainty in distributed model predictions using observed binary pattern information within GLUE, Hydrol. Process., 16, 2001–2016, 2002, https://doi.org/10.1002/hyp.398.

Arpae Emilia-Romagna: Rapporto degli eventi meteorologici di piena e di frana del 16–18 maggio 2023, Arpae Emilia-Romagna – Struttura Idro-Meteo-Clima, Bologna, 2023 (in Italian), available at: https://www.arpae.it/it/notizie/rapporto_idro_meteo_20230516-18.pdf.

ASCE/EWRI Task Committee on Dam/Levee Breaching: Earthen Embankment Breaching, J. Hydraul. Eng., 137, 1549–1564, 2011, https://doi.org/10.1061/(ASCE)HY.1943-7900.0000498.

https://doi.org/10.5194/egusphere-2026-2992
Preprint. Discussion started: 24 June 2026

Barbetta, S., Franchini, M., Melone, F., and Moramarco, T.: Enhancement and comprehensive evaluation of the Rating Curve Model for different river sites, J. Hydrol., 464–465, 376–387, 2012, https://doi.org/10.1016/j.jhydrol.2012.07.027.

Bates, P. D., Horritt, M. S., and Fewtrell, T. J.: A simple inertial formulation of the shallow water equations for efficient two-dimensional flood inundation modelling, J. Hydrol., 387, 33–45, 2010, https://doi.org/10.1016/j.jhydrol.2010.03.027.

Bates, P. D., and De Roo, A. P. J.: A simple raster-based model for flood inundation simulation, J. Hydrol., 236, 54–77, 2000, https://doi.org/10.1016/S0022-1694(00)00278-X.

Chang, D. S., Zhang, L. M., Xu, Y., and Huang, R. Q.: Field testing of erodibility of two landslide dams triggered by the 12 May Wenchuan earthquake, Landslides, 8, 321–332, 2011, https://doi.org/10.1007/s10346-011-0256-x.

Chow, V. T.: Open-channel hydraulics, McGraw-Hill, New York, 1959.

Dazzi, S., Vacondio, R., and Mignosa, P.: Integration of a Levee Breach Erosion Model in a GPU-Accelerated 2D Shallow Water Equations Code, Water Resour. Res., 55, 682–702, 2019, https://doi.org/10.1029/2018WR023826.

Dazzi, S., Vacondio, R., and Mignosa, P.: Internal boundary conditions for a GPU-accelerated 2D shallow water model: implementation and applications, Adv. Water Resour., 137, 103525, 2020, https://doi.org/10.1016/j.advwatres.2020.103525.

Dazzi, S., and Mignosa, P.: Flood hazard mapping in lowland areas: influence of treating artificial embankments as erodible elements, Hydrol. Sci. J., 71, 294–309, 2026, https://doi.org/10.1080/02626667.2025.2596261.

Deiana, C., Deidda, R., and Viola, F.: Geomorphic floodplain mapping in small Mediterranean catchments using LiDAR data, Adv. Water Resour., 178, 104493, 2023, https://doi.org/10.1016/j.advwatres.2023.104493.

Di Baldassarre, G., Castellarin, A., and Brath, A.: Analysis of the effects of levee heightening on flood propagation: example of the River Po, Italy, Hydrol. Sci. J., 54, 1007–1017, 2009, https://doi.org/10.1623/hysj.54.6.1007.

Di Baldassarre, G. and Montanari, A.: Uncertainty in river discharge observations: a quantitative analysis, Hydrol. Earth Syst. Sci., 13, 913–921, 2009, https://doi.org/10.5194/hess-13-913-2009.

Fell, R., Hanson, G., Herrier, G., Marot, D., and Wahl, T. Relationship between the erosion properties of soils and other parameters, in Erosion in geomechanics applied to dams and levees, edited by Bonelli S. and Nicot, F.), Wiley, 343–381, 2013, https://doi.org/10.1002/9781118577165.ch5.

Ferrari, A., Viero, D. P., Vacondio, R., Defina, A., and Mignosa, P.: Flood inundation modeling in urban areas: a mesh-independent anisotropic porosity approach, Adv. Water Resour., 125, 98-113, 2019, https://doi.org/10.1016/j.advwatres.2019.01.010.

Ferrari, A., Dazzi, S., Vacondio, R., and Mignosa, P.: Enhancing the resilience to flooding induced by levee breaches in lowland areas: a methodology based on numerical modelling, Nat. Hazards Earth Syst. Sci., 20, 59–72, 2020, https://doi.org/10.5194/nhess-20-59-2020

Ferrari, A., Vacondio, R., and Mignosa, P.: High-resolution 2D shallow water modelling of dam failure floods for emergency action plans, J. Hydrol., 618, 129192, 2023, https://doi.org/10.1016/j.jhydrol.2023.129192.

https://doi.org/10.5194/egusphere-2026-2992
Preprint. Discussion started: 24 June 2026

Ferrari, A., Passadore, G., Vacondio, R., Carniello, L., Pivato, M., Crestani, E., Carraro, F., Aureli, F., Carta, S., Stumpo, F., and Mignosa, P.: Hydrological and hydraulic investigation of the extreme September 2024 flood on the Lamone River in Emilia-Romagna, Italy, Nat. Hazards Earth Syst. Sci., 25, 2473–2479, 2025, https://doi.org/10.5194/nhess-25-2473-2025.

Froehlich, D. C.: Embankment dam breach parameters and their uncertainties, J. Hydraul. Eng., 134, 1708–1721, 2008, https://doi.org/10.1061/(ASCE)0733-9429(2008)134:12(1708).

Guan, M., Wright, N. G., and Sleigh, P. A.: 2D process-based morphodynamic model for flooding by noncohesive dyke breach, J. Hydraul. Eng., 140, 04014022, 2014, https://doi.org/10.1061/(ASCE)HY.1943 -7900.0000861.

Hanson, G. J. and Cook, K. R.: Apparatus, test procedures, and analytical methods to measure soil erodibility in situ, Appl. Eng. Agric., 20, 455–462, 2004, https://doi.org/10.13031/2013.16492.

Hanson, G. J. and Hunt, S. L.: Lessons Learned using Laboratory JET Method to Measure Soil Erodibility of Compact Soils, Appl. Eng. Agric., 23, 305–312, 2007, https://doi.org/10.13031/2013.22686.

Hanson, G. J. and Simon, A.: Erodibility of cohesive streambeds in the loess area of the midwestern USA, Hydrol. Process., 15, 23–38, 2001, https://doi.org/10.1002/hyp.149.

Hanson, G. J., Wahl, T. L., Temple, D., Hunt, S., and Tejral, R.: Erodibility characteristics of embankment materials, Proc. ASDSO Conf., 2010.

Horritt, M. S. and Bates, P. D.: Effects of Spatial Resolution on a Raster Based Model of Flood Flow, J. Hydrol., 253, 239–249, 2001, https://doi.org/10.1016/S0022-1694(01)00490-5.

Horritt, M. S., and Bates, P. D.: Evaluation of 1D and 2D numerical models for predicting river flood inundation, J. Hydrol., 268, 87–99, 2002, https://doi.org/10.1016/S0022-1694(02)00121-X.

Hosking, J. R. M. and Wallis, J. R.: Regional Frequency Analysis, Cambridge University Press, 1997.

Liang, Q. and Borthwick, A. G. L.: Adaptive quadtree simulation of shallow flows with wet-dry fronts over complex topography, Comput. Fluids, 38, 221–234, 2009, https://doi.org/10.1016/j.compfluid.2008.02.008.

Merz, B., Hall, J., Disse, M., and Schumann, A.: Fluvial flood risk management in a changing world, Nat. Hazards Earth Syst. Sci., 10, 509–527, 2010, https://doi.org/10.5194/nhess-10-509-2010.

Moramarco, T., Barbetta, S., Melone, F., and Singh, V. P.: Relating local stage and remote discharge with significant lateral inflow, J. Hydrol. Eng., 58–69, 2005, https://doi.org/10.1061/(ASCE)1084-0699(2005)10:1(58).

Morris, M. W., Hassan, M. A. A. M., and Vaskinn, K. A.: Breach formation: field tests and laboratory experiments, J. Hydraul. Res., 45, Suppl. 1, 9–17, 2007, https://doi.org/10.1080/00221686.2007.9521828.

Neal, J., Schumann, G., and Bates, P.: A subgrid channel model for simulating river hydraulics and floodplain inundation over large and data sparse areas, Water Resour. Res., 48, W11506, 2012, https://doi.org/10.1029/2012WR012514.

Nguyen, V. N., Courivaud, J. R., Pinettes, P., Souli, H., and Fleureau, J. M.: Using an Improved Jet-Erosion Test to Study the Influence of Soil Parameters on the Erosion of a Silty Soil, J. Hydraul. Eng., 143, 04017018, 2017, https://doi.org/10.1061/(ASCE)HY.1943-7900.0001305.

https://doi.org/10.5194/egusphere-2026-2992
Preprint. Discussion started: 24 June 2026

Papaioannou, G., Efstratiadis, A., Vasilades, L., Loukas, A., Papalexiou, S. M., Koukouvinos, A., Tsoukalas, I., and Kossieris, P.: An operational method for Flood Directive implementation in ungauged urban areas, Hydrology, 5, 24, 2018, https://doi.org/10.3390/hydrology5020024.

Pappenberger, F., Beven, K. J., Horritt, M., and Blazkova, S.: Uncertainty in the calibration of effective roughness parameters in HEC-RAS using inundation and downstream level observations, J. Hydrol., 332, 46–69, 2005, https://doi.org/10.1016/j.jhydrol.2004.06.036.

Petersen-Øverleir, A.: Accounting for heteroscedasticity in rating curve estimates, J. Hydrol., 292, 173–181, 2004, https://doi.org/10.1016/j.jhydrol.2003.12.024.

Partheniades, E.: Erosion and deposition of cohesive soils, J. Hydraul. Div., 91, 105–139, 1965, https://doi.org/10.1061/JYCEAJ.0001165.

Regione Emilia-Romagna: Rapporto della Commissione tecnico-scientifica istituita con deliberazione della Giunta Regionale n. 984/2023 e determinazione dirigenziale 14641/2023, al fine di analizzare gli eventi meteorologici estremi del mese di maggio 2023, Regione Emilia-Romagna, Bologna, 2023 (in Italian), available at: https://www.regione.emilia-romagna.it/alluvione/rapporto-della-commissione-tecnico-scientifica.

Rogers, B. D., Borthwick, A. G. L., and Taylor, P. H.: Mathematical balancing of flux gradient and source terms prior to using Roe's approximate Riemann solver, J. Comput. Phys., 192, 422–451, 2003, https://doi.org/10.1016/j.jcp.2003.07.020.

Schubert, J. E. and Sanders, B. F.: Building treatments for urban flood inundation models and implications for predictive skill and modeling efficiency, Adv. Water Resour., 41, 49–64, 2012, https://doi.org/10.1016/j.advwatres.2012.02.012.

Song, Y., Huang, J., Toorman, E., and Yang, G.: Reconstruction of River Topography for 3D Hydrodynamic Modelling Using Surveyed Cross-Sections: An Improved Algorithm, Water, 12, 3539, 2020, https://doi.org/10.3390/w12123539.

Tavares da Costa, R., Manfreda, S., Luzzi, V., Samela, C., Mazzoli, P., Castellarin, A., and Bagli, S.: A web application for hydrogeomorphic flood hazard mapping, Environ. Model. Softw., 118, 172–186, 2019, https://doi.org/10.1016/j.envsoft.2019.04.010.

Toro, E. F.: Riemann Solvers and Numerical Methods for Fluid Dynamics, Springer, 1999.

Vacondio, R., Dal Palù, A., Mignosa, P., and Aureli, F.: GPU-enhanced Finite Volume Shallow Water solver for fast flood simulations, Environ. Model. Softw., 57, 60–75, 2014, https://doi.org/10.1016/j.envsoft.2014.02.003.

Vacondio, R., Dal Palù, A., Ferrari, A., Mignosa, P., Aureli, F., and Dazzi, S.: A non-uniform efficient grid type for GPU-parallel Shallow Water Equations models, Environ. Model. Softw., 88, 119–137, 2017, https://doi.org/10.1016/j.envsoft.2016.11.012.

Vorogushyn, S., Merz, B., and Apel, H.: Development of dike fragility curves for piping and micro-instability breach mechanisms, Nat. Hazards Earth Syst. Sci., 9, 1383–1401, 2009, https://doi.org/10.5194/nhess-9-1383-2009.

Wahl, T. L.: Prediction of Embankment Dam Breach Parameters, DSO-98-004 Dam Safety Research Report, 1998.

Wu, W.: Simplified physically based model of earthen embankment breaching, J. Hydraul. Eng., 139, 837–851, 2013, https://doi.org/10.1061/(ASCE)HY.1943-7900.0000741.